# Irrigation contrasts through the morning transition

J K Brooke, M J Best, A P Lock, S R Osborne, J. Price, J. Cuxart, Aaron Boone, G. Canut-Rocafort, O K Hartogensis, A. Roy

ORIGINAL ARTICLE

Journal Section

# Irrigation contrasts through the morning transition

J. K. Brooke[1] | M. J. Best[1] | A. P. Lock[1] | S. R. Osborne[2] | J. Price[2] | J. Cuxart[3] | A. Boone[4] | G. Canut-Rocafort[4] | O. K. Hartogensis[5] | A. Roy[4]

[1]Met Office, FitzRoy Way, Exeter, EX1 3PB.

[2]Met Office Field Site, Cardington Airfield, Bedford, MK42 0SY.

[3]University of Balearic Islands, Spain

[4]CNRM - Université de Toulouse, Météo-France/CNRS

[5]Meteorology and Air Quality Group, Wageningen University and Research, 6708 PB, Wageningen, The Netherlands

**Correspondence**
Met Office, FitzRoy Way, Exeter, EX1 3PB.
Email: jennifer.brooke@metoffice.gov.uk

**Funding information**

The Land surface Interactions with the Atmosphere over the Iberian Semi-arid Environment (LIAISE) campaign was conducted in July 2021 primarily to investigate the role of irrigation in modulating the boundary layer evolution in the Catalan region of northeastern Spain. Contrasts in near-surface meteorological parameters and boundary layer thermodynamic profiles at an irrigated and rainfed (arid) site were established during the morning transition. Evapotranspiration dominated the flux partitioning at the irrigated site (Bowen ratio of 0.07–1.1), whilst sensible heat flux dominated at the rainfed (arid) site (Bowen ratio greater than 10.0). The cumulative evapotranspiration during July 2021 was a factor of 10 greater at the irrigated site than at the rainfed (arid) site. The presence of irrigation was shown to modulate the vertical gradients of turbulence, temperature, and moisture. Irrigation is shown to have a significant effect on the development of the boundary layer including during the morning transition. The morning transition mean buoyancy flux was 2.8 times smaller at the irrigated site (1.1 $m^2$ $s^{-2}$) compared with the rainfed (arid) site (3.1 $m^2$ $s^{-2}$), with a resultant delay in the near-surface buoyancy-flux crossover time (30-min to 90-min) at the irrigated site. At the start of the morning transition (sunrise), the average screen-level (50 m) temperature was -1.2 K (-1.9 K) colder at the irrigated site relative to the rainfed (arid) site. The colder temperatures at sunrise at the irrigated site are predominately the result of colder boundary layer thermodynamic profile from the previous day. At the end of the morning transition (convective onset), temperature differences between the two sites extend through much of the boundary layer and increased in magnitude. The average screen-level (50 m) temperature difference was -3.6 K (-2.4 K) colder at the irrigated site relative to the rainfed (arid) site. There was considerable day-to-day variability in temperature contrasts at a regional level (-2.4 to -6.0 K).

**KEYWORDS**
Semi-arid, buoyancy flux, convective onset, turbulence, thermodynamic profiles, LIAISE

## 1 | INTRODUCTION

In semi-arid and arid regions, water availability in the landscape can be altered by human management processes, such as irrigation. This has enabled agricultural regions to expand into areas previously unable to support food production, and to increase crop productivity and yields (Valmassoi and Keller, 2022). The Intergovernmental Panel on Climate Change (IPCC) Special Report on *Climate Change and Land* states that globally the total production of food has increased by 240 %, and the use of irrigation water and irrigated area has doubled *(high confidence)* between 1961 and 2017 (Arneth et al., 2019).

Irrigation practices vary across agriculture practices and processes include flood/gravity irrigation, drip irrigation and sprinkler. The method of irrigation can strongly influence the frequency and duration of moisture availability. The addition of moisture to the surface has implications for the energy partitioning at the surface, which defines the Bowen ratio (the ratio of sensible to latent heat flux). There is *very high confidence* (Jia et al., 2019) that irrigation increases total evapotranspiration, reduces crop stress (Zaveri and Lobell, 2019), increases the total amount of water vapour in the atmosphere (de Vrese and Hagemann, 2018) and decreases mean surface daytime temperature within the irrigated area (Lawston et al., 2020).

Away from irrigated regions, evapotranspiration from natural vegetation over semi-arid regions is highly sensitive to the soil moisture availability. This can further enhance contrasts in the land surface variability (including the distribution of vegetation cover and leaf area index) and give rise to greater surface heterogeneity.

Irrigation processes are not widely represented, or treated simplistically, in numerical weather prediction systems and in general circulation models (Lobell et al., 2006). The Coupled Model Intercomparison Project (Phase 6) (CMIP6) climate models, for example, include a basic representation of land-use and land cover change, but very few include irrigation. This can give rise to systematic warm-and-dry simulation biases (Barton et al., 2023). Studies have shown that the cooling effects of irrigation may be underestimated by global climate models due to their coarse spatial resolutions (Sorooshian et al., 2011; Chen and Dirmeyer, 2020). Irrigation datasets are required to both model and evaluate irrigation schemes and parameterizations, with information required for four key properties of irrigation: where, when, how, and how much to irrigate (Xia et al., 2022).

Studies have shown that models incorrectly simulate the surface flux partitioning related to the treatment of irrigation, not explicitly included in the model (Cuxart et al., 2015). Increased evapotranspiration over irrigated areas has been shown to have a complex interaction with boundary layer processes and growth. For example, surface-flux contrasts can lead to the generation of secondary circulations (Legain et al., 2013; Cuxart et al., 2012) that can alter the depth and structure of the boundary layer, whilst complex mixed layers arising from surface heterogeneity can provide a capping inversion that suppresses boundary layer growth (Lanicci et al., 1987; Reen et al., 2014). Observation datasets for land surfaces with different soil moisture (e.g. driven by antecedent rainfall patterns) have previously offered insight into the role of soil moisture in modulating the boundary layer development. Barton et al. (2019) demonstrated evidence that soil moisture heterogeneity drives mesoscale circulations with observations of divergent (convergent) wind flow above wetter (drier) surfaces, suppression of shallow cloud above wetter soils and wet–dry soil moisture boundaries predominantly favouring the initiation of deep convection.

The Special Report on *Climate Change and Land* states with *high confidence* (Shukla et al., 2019) that water avail-

ability from irrigation practices will affect climate in regions as far as few hundreds of kilometres downwind (Cook et al., 2011; Thiery et al., 2020). Mangan et al. (2023) examined surface-boundary layer interactions across spatial scales of irrigation-driven thermal heterogeneity finding at the regional scale observed boundary-layer properties could be explained through a composite of surface fluxes, whereas at the local scale non-local advection processes are important for partitioning energy. Some larger-scale interactions are less well understood, such as the impact on entrainment rates impacting on the boundary layer growth, and feedbacks and interactions with convection, cloud formation and precipitation (Reen et al., 2014; Lawston et al., 2015). The impact of irrigation on the established convective boundary layer has received focused attention (Rappin et al., 2021; Lawston et al., 2020). Studies typically focus on a well established convective boundary layer, where contrasts arising from irrigation are expected to be larger, with a more dominant signal. To our knowledge studies have not focused on the impacts of irrigation during the morning transition period, and in doing so neglect understanding the processes which are critical to the development of the convective boundary layer. The morning (and evening) transition period is an evolution from a nocturnal, statically stable boundary layer to a convective boundary layer (and vice versa).

One of the first processes acting to drive this transition is a positive near-surface buoyancy flux, driven by solar heating. The time of crossover (a change in sign from a negative buoyancy flux to a positive buoyancy flux) is an important reference point in the morning transition period (Angevine et al., 2001). The morning transition covers a period of time starting with sunrise and ending when two processes have occurred; the first being an observation of turbulence substantially above the surface (Hogan et al., 2009) and secondly an erosion of the near-surface temperature inversion (Angevine et al., 2001). The latter event is called convective onset.

Angevine et al. (2020) led a recent overview of the transition periods over land focusing on key processes in the atmospheric boundary layer as it undergoes transitions between stable and convective states. The review called for new multi-scale networks of observations to provide insight into the influence of surface heterogeneity and horizontal variations in surface characteristics on transitional boundary layers.

This paper proposes to fill this gap, focusing on the impacts of irrigation on the morning transition, by using observations collected from the 2021 Land surface Interactions with the Atmosphere over the Iberian Semi-arid Environment (LIAISE) campaign (Boone et al., 2021). The LIAISE campaign was located in the Urgell and Pla d'Urgell in the Catalan region of northeastern Spain, incorporating the Ebro river basin. The campaign took place during June through October 2021. The region has a significant irrigation presence surrounded by a naturally rainfed region, which is arid during the summer months. During July 2021, a two-week Special Observing Period (SOP) occurred with intensive measurements across the study region including a surface network of eddy-covariance flux towers. We make particular use of hourly radiosonde soundings during the morning transition period to allow us to contrast boundary-layer thermodynamic profiles at two supersites, one located in the irrigated region and one located in the rainfed (arid) region. These observations will enable the examination of the role of irrigation in modulating surface moisture content, the impact on surface heat fluxes, and subsequent interactions and feedback on the boundary layer evolution.

This article is arranged as follows: Section 2 provides a description of the study region with a focus on the instrumentation deployed at two supersites, and an overview of the Intensive Observation Periods (IOPs) which occurred during the two-week SOP. Results are presented in Section 3 which contrasts the evolution of sub-surface and sur-

face conditions, and near-surface and boundary-layer structure in the irrigated and naturally rainfed regions. Section 4 presents the conclusions.

# 2 | METHODOLOGY

## 2.1 | LIAISE Study Region

The LIAISE study region covers approximately a 30x30 km square area and had two clearly defined zones; one that is irrigated and one that is naturally rainfed, but arid during the summer months. The two zones are divided by an irrigation canal (divided from southwest to northeast). A network of 8 eddy-covariance flux sites were deployed across the region during July 2021; 5 land surface sites located in the irrigated zone and 3 sites located in the rainfed zone. Each site was selected to be representative of a different dominant crop grown in the region or the natural vegetation, and provide a measure of the surface heterogeneity.

A map of the study region including the flux site locations is presented in Figure 1a which highlights the irrigated region from the ESA Climate Change Initiative Land Cover (ESA CCI LC) [1] dataset. Also presented is the regional orography from the Global Multi-resolution Terrain Elevation Data 2010 (GMTED2010) [2] dataset. The predominant orography influencing the region is the Catalan pre-coastal range to the south and south-west of the LIAISE study region which runs parallel to the Mediterranean Sea coast in Catalonia. One notable sub-range is the Serra del Terrat range to the south-west which will be discussed in section 2.2 in the context of the arrival of an afternoon sea breeze. On a larger scale (not shown) the region has topographical barriers of the Pyrenees to the north and the Iberic System to the southwest.

This study will focus on the observations at two LIAISE supersites, one located in the rainfed zone (Els Plans, section 2.1.1) and the other located in the irrigated zone (La Cendrosa, section 2.1.2). The two supersites are located approximately 15 km apart (Boone et al., 2021). A third supersite (Mollerusa, mixed orchard) was located in the irrigated zone although observations from this site will not be used in this study.

### 2.1.1 | Els Plans site: winter crops and seasonal bare soil (rainfed zone)

The Els Plans site (41°35′22.25′′$N$, 1°1′48.00′′$E$) (hereafter referred to as rainfed site) is one of two supersites deployed during LIAISE, located in the rainfed zone. The vegetation at the site is combination of winter crops and natural vegetation. During the driest months of year, this region has significant bare soil and senescent vegetation. The site elevation is 335 m above mean sea level. The site consists of a 50 m flux tower installation (deployed by the Met Office), with sensors located at 1.2, 10, 25 and 50 m. Figure 1(i) presents a photo of the rainfed site with the 50 m flux tower installation taken during the SOP in July 2021. Air temperature, relative humidity, and winds at all heights are measured with Vector Instruments T302, Vaisala HMP155 sensors (both housed in aspirated screens) and Gill HS50

[1] http://maps.elie.ucl.ac.be/CCI/viewer/download/ESACCI-LC-Ph2-PUGv2_2.0.*pdf*

[2] https://www.usgs.gov/publications/global-multi-resolution-terrain-elevation-data-2010-gmted2010

3D ultrasonic anemometers, respectively. Hemispherical shortwave radiative fluxes and long-wave irradiance are measured with a Kipp and Zonen CM21 pyranometer and Kipp and Zonen CGR4 pyrgeometer, respectively. Rainfall is measured with a Met Office Mk5 tipping-bucket gauge with a 0.2 mm accuracy.

Sensible heat and momentum fluxes are measured at all of the flux tower heights based on 10-Hz data. Latent heat flux is measured at 2 m and 10 m with a Krypton hygrometer and Licor Li-7500 open-path hygrometer, respectively. Eddy covariances over 10- and 30-min intervals were used to calculate the turbulent heat and moisture fluxes, and buoyancy flux. Data at 10-min intervals from 2 m observations is used to determine the timings of the buoyancy flux crossover. The sonic data has cross-wind speed correction, coordinate rotation, detrending and despiking applied.

The grass canopy air temperature and relative humidity is determined in-situ with a screened and aspirated Rotronic Hydroclip2 at 8 cm nominal height. Volumetric soil moisture was measured at five depths. A Delta-T ML3 probe measured volumetric soil moisture at 2 and 10 cm and a Delta-T PR2 probe measured at 20, 30, and 40 cm. A Delta-T ST2-396 thermistor probes measure soil temperature at 1, 4, 10, 17, and 35 cm.

A number of instruments at the site were deployed for measurements of the atmospheric boundary layer. Specifically used in the study, a 1.5 $\mu$m Halo Photonics Streamline lidar (Pearson et al., 2009) measures radial backscatter and doppler velocity from aerosol. The Halo was operated with a zenith view and so vertical velocity and the vertical component of turbulence, as well as the boundary-layer structure, were continuously monitored. The vertical resolution of the Doppler lidar is 18 m, and the lower boundary of the first usable gate is 108 m. The vertical velocity variance from the Halo Doppler lidar can be combined with the vertical velocity variance from the tower heights to provide a profile from the near surface (2 m) through the boundary layer to the maximum detection limit of the Halo Doppler lidar.

Atmospheric vertical profiles (to a maximum height of 8 km) were obtained with Vaisala RS92-SGP radiosondes. Sondes were launched hourly starting before sunrise (0400 UTC) and ending at 1700 UTC. Further details of the radiosonde launch strategy are provided in section 2.2.

### 2.1.2 | La Cendrosa site: irrigated Alfalfa (irrigated zone)

The La Cendrosa site (41°41′35.89″$N$, 0°55′42.20″$E$) (hereafter referred to as irrigated site) is the second supersite deployed during LIAISE located in an alfalfa crop within the irrigated zone. Alfalfa is a rapidly growing crop with multiple harvests in a growing season; the crop was cut (6 July) prior before the start of the two-week SOP, and had a height of approximately 70 cm by the end of the SOP. La Cendrosa is irrigated using a flood/gravity method, typically having two irrigation events per alfalfa harvest. Irrigation was applied just before and once during the SOP on 11 July and 24 July 2021, respectively. The site elevation is 239 m above mean sea level.

The site consists of a 50 m flux tower installation (deployed by Centre National de Recherches Météorologiques), with sensors located at 0.2, 2, 10, 25 and 45 m. Figure 1(h) presents a photo of the irrigated site with the 50 m flux tower installation taken during the SOP in July 2021. Air temperature and relative humidity at all heights are measured with Thermoest PT100 and Vaisala HMP110 sensors (both housed in aspirated screens). For wind speed and direction, a Young Wind Monitor provides measurements at 10 m, Gill Horizontal Research 1199-PK-102 3D ultrasonic

anemometers are positioned at 3 and 25 m and Gill R3-50 1210-PK-085 3D ultrasonic anemometer is positioned at 50 m. Four-component radiation measurements at 1 m are obtained with Kipp and Zonen CNR4 net radiometer which consists of a pyranometer pair, one facing upward, the other facing downward, and a pyrgeometer pair in a similar configuration. Rainfall is measured with a Précis Mécanique 3039 which measured accumulation of rainfall between two consecutive timestamps. Thermoest PT100 and Delta T thetaprobe ML3 measures soil temperature and volumetric soil moisture at three depths of 5, 10 and 30 cm.

A second 2 m Campbell Scientific IRGASON eddy covariance system consisting of a CSAT3 sonic with an integrated, open-path infra-red gas analyzer operated at 20 Hz was installed at La Cendrosa. This system was deployed by the University of Wageningen, although sited differently (east of the main 50 m flux tower) within the alfalfa crop.

A Leosphere WindcubeV2 lidar provides vertical wind profiles and turbulent kinetic energy (TKE) profiles for the lowest 220 m. The vertical resolution of the Leosphere WindcubeV2 lidar is 20 m, and the lowest measured gate is centred at 40 m.

A coordinated radio sounding strategy was developed between the two supersites. At the irrigated site two types of radiosondes were deployed; a conventional sounding was made at 0700 UTC and 1700 UTC with Vaisala RS41-SGP receiver and all other soundings used a reusable capability with RS92-SGP receivers. The reusable sounding technique has been developed by CNRM, with comprehensive details in Legain et al. (2013). The system is adapted from conventional soundings and uses two balloons with different inflated volumes; a larger volume for the ascent and a small volume to provide a controlled descent. The ascent balloon is released by a cutting system at a programmed maximum height which allows the sonde to be recovered and reused. The programmed maximum height typically ranged from 3 km, which enabled complete soundings of the boundary layer and also minimised the recovery distance of the sonde.

## 2.2 | LIAISE Intensive Observing Periods (IOPs)

In total, eleven IOPs were obtained and a summary is presented in Table 1 providing the dates, radiosonde timings, and weather conditions for each IOP discussed within this study. A radiosonde strategy was developed where simultaneous soundings were carried out at the rainfed and irrigated site with hourly launches between 0400 UTC and 1700 UTC during each IOP. Hourly soundings were a priority for IOPs to observe the evolution of the thermodynamic profiles. On four IOPs, soundings were extended into evening transition at the rainfed site, ending at 2100 UTC. A total of 269 radiosondes were launched, with 11 IOPs (154 radiosondes) and 7 IOPs (115 radiosondes) at the irrigated and rainfed sites, respectively. In this study we focus our analysis on 15–17 July (IOP1–3), 19 July (IOP4, although radiosondes are only available for the irrigated site), 20–22 July (IOP5–7) and 27 July (IOP10).

Generally, all IOP days generally had clear skies. In this study, we identify three meteorological flow regimes and split the IOPs accordingly. Firstly, IOP1–4 are predominately influenced by synoptic-scale westerly flow. In the Ebro basin, winds from the north and west are forced by the topographical barriers of the Pyrenees (to the north) and the Iberic System (to the southwest). This flow is established shortly after sunrise and near-surface winds are generally light (2–4 m $s^{-1}$ between 2 m and 50 m). Figure 1 (b) and (e) presents windrose plots at 2 m showing wind

direction and speed during the morning transition at the rainfed and irrigated sites for synoptic-scale westerly flow IOPs (regime 1). The plots highlight the near-surface flow at both sites is similar in terms of wind direction and wind speed. Wind speeds generally increase (4–6 m $s^{-1}$ between 2 m and 50 m) in the late afternoon with the arrival of a sea breeze front. The sea breeze front is the arrival of wind from the Catalan coast driven by a pressure difference created due to the different heat capacities of the land surface and sea. The progression of the sea breeze front is slowed by the presence of the Catalan pre-coastal range and Serra del Terrat range. The sea breeze front arrival is earlier (IOP1–3 average 30-min earlier) at the rainfed site, due to its more south-westerly location. A summary of the sea breeze duration for each IOP is included in Table 1.

In the second regime, a thermal low is established across the region during IOP5–7 where anticyclonic flow dominates the circulation up to a height of 500 hPa. Cuxart et al. (2012) proposed a mechanism for the formation of this regime; at times with no well-defined synoptic pressure gradients in the area, locally generated flow develops due to thermal differences at the surface. The irrigated zone has a suppressed temperature diurnal cycle compared with the surrounding rainfed zone, due to the increased heat capacity due to the higher water content of the irrigated soil and larger evaporative cooling during day. This allows greater morning heating and evening cooling to take place over the rainfed zone at a higher rate than over the irrigated zone, therefore amplifying the classical diurnal circulation. The average time of the sea breeze front arrival during the thermal low regime (IOP5–7) was found to be earlier (1300 UTC at the rainfed site, and 1530 UTC at the irrigated site), suggesting that the sea breeze front propagates more quickly during this flow regime plot not shown).

Figure 1 (c) and (f) presents windrose plots at 2 m showing wind direction and speed during the morning transition at the rainfed and irrigated sites, respectively, for the thermal low IOPs (regime 2). The irrigated site is influenced more predominately by north-easterly flow, whilst the rainfed site receives from from a south-easterly direction which is generally aligned with down-slope flows from the Serra del Terrat range. The near-surface winds during the morning transition are seemingly disconnected between the two sites. Without the presence of synoptic scale westerly flow, local nocturnal flows are established, and the direction of these winds are strongly influenced by local topography. These local nocturnal flows predominate over the flow during the morning transition period.

In the third regime, IOP10 is influenced by anticyclonic flow below 850 hPa and westerly flow at 500 hPa. The influence of the thermal low has weakened. Figure 1 (d) and (g) presents equivalent windrose plots for anticyclonic flow (regime 3) at the rainfed and irrigated sites. Noticeably, wind speeds during the morning transition are lower during anticyclonic regime compared with regime 1 or 2. Similar to regime 2, the wind direction during the anticyclonic is strongly influenced by local topography.

## 3 | RESULTS

### 3.1 | July 2021 evolution

The evolution of volumetric soil moisture content, Bowen ratios, cumulative evapotranspiration and precipitation during July 2021 at the irrigated and rainfed sites are presented in Figure 2. The IOP days are shown by the vertical

pink lines so this provides context to the conditions in the preceding two-weeks before the start of the SOP.

Figure 2a contrasts the evolution of volumetric soil moisture content in the top 30 cm of the soil for the irrigated site and the top 10 cm of soil at the rainfed site. Additionally presented are the moisture contents at saturation and the critical and wilting points (presented as black dashed lines on Figure 2a). Soil information (soil unit identifier) for the two sites is taken from the Harmonised World Soil Database (HWSD). Soil unit identifier 863 accounted for 35 % and soil unit identifier 922 accounted for 65 % of the soil type at the site locations. Each soil unit is assigned a sand/silt/clay fractions in the database which have been used with pedotransfer functions to determine soil parameters.

At the rainfed site, the soil moisture content is less than 10 % and 14 %, at 2 cm and 10 cm, respectively. The minimum soil moisture reached during the SOP is 5 % (at 2 cm) on the 25 July, although precipitation on the 26 July (prior to IOP10) leads to a small increase in soil moisture. No response in soil moisture at 10 cm is evident to the precipitation event. Examining the volumetric soil moisture content at the irrigated site, the most notable changes are seen on 11 July and 24 July, when (flood) irrigation is applied to the alfalfa crop. A sharp increase in soil moisture at all three soil depths is observed with a saturation of soil moisture at 40 % and 48 %, for the 5 cm and 10 cm levels, respectively. The saturated conditions do not persist at either level and a rapid drying of the soil moisture content is seen on the day the irrigation is applied. A gradual decrease in soil moisture is evident between IOP1 (27 %) and IOP7 (20 %) between the irrigation events. This corresponds to transition from the critical point to the wilting point between irrigation events.

Two precipitation events occurred during the two-week SOP, summarised in Figure 2d, which are important to highlight as these affect the kinematic buoyancy flux on subsequent IOP days (the analysis of which will be presented in 3.2). The first precipitation event was a short 1.5-hour convective period overnight on 20–21 July (IOP5–6) with 1.6 kg $m^{-2}$ and 0.6 kg $m^{-2}$ cumulative precipitation at the irrigated and rainfed site, respectively. The second precipitation event on 26 July was associated with a frontal passage, and no intensive observations were made on this day. The cumulative precipitation was 32.0 kg $m^{-2}$ and 3.4 kg $m^{-2}$ at the irrigated and rainfed site, respectively.

Figure 2b contrasts the Bowen ratio at the two sites. At the rainfed site, the Bowen ratio is greater than 10.0 for all days in July (apart from 26 July which is associated with a frontal system) indicating sensible heat flux dominates the flux partitioning. At the irrigated site, Bowen ratios range from 1.1 (IOP1, 15 July) to 0.07 (IOP7, 22 July). This indicates that at the beginning of the SOP a greater proportion of the available energy at the surface is employed as sensible heat flux than latent heat flux, with a transition to being dominated by latent heat flux in the later stages of the SOP. The irrigated canopy height growth is shown in Figure 2b indicating growth from 10 cm on 11 July to 70 cm on 28 July, at the end of the SOP. The observed changes in the Bowen ratio can be explained, firstly by the growth of the canopy height during the SOP which results in increasing evapotranspiration and secondly, a denser vegetation canopy which naturally reduces the heat flux from the soil surface.

The differences between the two sites are further emphasised in Figure 2c which contrasts the cumulative evapotranspiration. The cumulative evapotranspiration during July at the irrigated site is 69.9 kg $m^{-2}$ (72.0 kg $m^{-2}$) at 3 m (50 m), and is a factor of 10 greater than at the rainfed site (5.6 kg $m^{-2}$ and 8.8 kg $m^{-2}$ at 2 m and 10 m, respectively). For the first half of July, the cumulative evapotranspiration at the irrigated site is greater at 50 m than 3 m, signifying a greater non-local source of evapotranspiration. In the second half of July, a change between the two heights is seen,

with cumulative totals at 3 m which are larger than 50 m. This further highlights the impact of the growing canopy height during the SOP and the increasing dominance of field scale evapotranspiration.

## 3.2 | Kinematic buoyancy flux

Figure 3 presents the observed diurnal cycle of the kinematic buoyancy flux, i.e. the turbulent heat flux calculated with the virtual potential temperature including the moisture flux contribution. Data at 10-min intervals from 2 m observations from both supersite locations are used to determine the timings of the buoyancy flux crossover. We define crossover as the change in sign of the near-surface (2 m) buoyancy flux, i.e. when the flux becomes positive (0.1 W $^{-2}$). Table 2 summarises the morning buoyancy-flux crossover times, for the irrigated and rainfed sites, at each of the tower heights. The time of sunrise is included as a point of reference, marking the start of the morning transition period.

At the irrigated site two near-surface flux measurements were deployed. The first installation (3 m) on the 50 m flux tower was deployed at the west of the irrigated site (deployed by Centre National de Recherches Météorologiques), and the second installation (2 m) was a separate 2 m flux tower deployed at the east of the irrigated site by the University of Wageningen. This siting difference within the alfalfa crop (the Wageningen site being more central within the alfalfa crop) has led to discernible differences in the near-surface buoyancy-flux crossover times as evident in Figure 3. The 2 m buoyancy flux is consistently smaller in magnitude compared to the 3 m buoyancy flux, particularly evident during IOP1–4, and is predominately driven by heterogeneity in the canopy height and canopy cover of the alfalfa crop particularly in the early stages of growth of alfalfa after the cutting stage.

On all IOP days there is a delay in the buoyancy-flux crossover time at the irrigated site relative to the rainfed site (Table 2). This delay is evident at all heights up to 50 m on the flux tower. This reflects the difference in energy partitioning between the irrigated and rainfed (arid) surfaces. Irrigation decreases (increases) the sensible (latent) heat flux, reducing the Bowen ratio, which in turn suppresses the near-surface turbulence generation and decreases the buoyancy-flux. The meteorological flow regime played a role in the variability of the buoyancy-flux crossover time delay. For synoptic scale westerly flow days (IOP1–4) the average delay at 2 m (50 m) in crossover time was 30-min (50-min), whilst for thermal low regime (IOP5–7) and anticyclonic regime (IOP10) the average delay in crossover time was almost 90-min (58-min) longer at the irrigated site.

The mean difference in crossover time between 2 m and 50 m at the rainfed site is 20-min for synoptic scale westerly flow days (IOP1–4), compared with 40-min for thermal low and anticyclonic regimes (IOP5–7&10). This suggests that near-surface turbulence generation occurs more quickly on days with synoptic scale westerly flow, than during the thermal low regime. The mean difference in crossover times between 2 m and 50 m at the irrigated site is 2[illegible]-min for IOP1–4, compared with 37-min for IOP5–7&10. The largest delay in a positive heat flux occurs on IOP7 where there is a 70-min (90-min) difference in the buoyancy-flux crossover point between 2 m and 50 m at the rainfed (irrigated) site.

Table 3 contrasts the mean buoyancy-flux during the morning transition between the two sites. The buoyancy flux at the rainfed site was 2.8 times the magnitude of the buoyancy flux at the irrigated site. The morning transition

mean buoyancy flux was 1.1 $m^2\ s^{-2}$ and 3.1 $m^2\ s^{-2}$ for the irrigated and rainfed site, respectively. Table 3 additionally compares the latent heat flux contribution to the buoyancy flux during the morning transition. At the rainfed site, the latent heat flux contribution to the buoyancy flux during IOP1–4 was less than 1.3 % with the buoyancy flux almost entirely dominated by the sensible heat flux. During IOP5–7&10, the latent heat flux contribution was in the range of 1.0–5.3 % at 2 m and 2.1–10.1 % at 25 m. The percentage contribution increases with increasing tower height and increasing measurement fetch, indicating a non-local source of water vapour.

In contrast, at the irrigated site, the latent heat flux contribution to the buoyancy flux is more variable, predominately driven by the growth of the irrigated vegetation canopy during the two-week SOP. During IOP1–4, the latent heat flux contribution was in the range of 10–30 %, whilst during IOP5–7 over a three day consecutive period the latent heat flux contribution to the 2 m (50 m) buoyancy flux is seen to have a significant increase from 37 % (25 %) to over 90 % (83 %). At the irrigated site, the smallest measured Bowen ratio occurred on IOP7 (0.07) which coincided with the largest latent heat flux contribution to the 2 m buoyancy flux (90 %). The latent heat flux contribution to the buoyancy flux is also seen to respond to temperature variability across the IOPs, with the highest latent heat flux contribution occurring during the thermal low regime IOP days. IOP10 in contrast has a latent heat flux contribution more consistent with that of IOP4&5 (25–37 %).

Table 4 examines the latent heat flux contribution to the buoyancy flux for the middle of the day (calculated for 1000–1400 UTC) to understand if the contrasts between the two sites, and trends between IOPs, observed in the morning transition period extend throughout the daytime period. At the rainfed site, the latent heat flux contribution to the buoyancy flux was less than 1.0 % in the middle of the day on all IOPs, and an even smaller contribution than during the morning transition. The variability in the morning transition period during both the thermal low and anticyclonic regimes (IOP5–7&10) is not evident in the middle of the day at the rainfed site.

At the irrigated site, the trends discussed previously appear to be consistent between the morning transition and middle of the day. During the synoptic scale westerly flow regime (IOP1–3), the buoyancy flux at the rainfed site was 2.6 times greater than at the irrigated site. The daily mean (1000–1400 UTC) buoyancy flux was 3.9 $m^2\ s^{-2}$ and 10.1 $m^2\ s^{-2}$ for the irrigated and rainfed site, respectively. During the thermal low and anticyclonic regime (IOP5-7), the buoyancy flux at the rainfed site accounted for 5 times the buoyancy flux at the irrigated site. The daily mean (1000–1400 UTC) buoyancy flux was 1.6 $m^2\ s^{-2}$ and 8.9 $m^2\ s^{-2}$ for the irrigated and rainfed site, respectively.

## 3.3 | Vertical velocity variance and skewness

The variance of the vertical velocity ($\sigma_w^2$) is a measure of the vertical intensity of turbulence. Identifying a number of heights with observations of vertical velocity variance, it is possible to examine the propagation and vertical growth of turbulence through the morning transition. Figure 4 examines the observed vertical velocity variance using observations at heights from 2 m to 50 m to contrast the vertical intensity of turbulence at the rainfed and irrigated sites. Previous studies have defined the time of convective onset to be where the variance in vertical velocity at a height of 200 m, as measured with a Halo Doppler lidar, is greater than 0.12 $m^2\ s^{-2}$ when combined with a positive skewness (Brooke and Osborne, 2021; Hogan et al., 2009). Firstly, we examine if the vertical velocity threshold is applicable to

the 50 m observations on the flux tower and secondly explore differences in the vertical velocity variances at the two sites.

Applying the 0.12 $m^2\ s^{-2}$ threshold described to the vertical velocity variance at 50 m, it is found the average time that the variance threshold is exceeded at 50 m during the synoptic scale westerly flow cases (IOP1–3) is 100-min (0525 UTC) and 130-min (after sunrise) (0655 UTC), for the rainfed and irrigated sites, respectively. This gives rise to a 30-min delay at 50 m at the irrigated site compared with the rainfed site. For the thermal low regime (IOP5–7), the average time that the variance threshold is exceeded at 50 m is 110-min (0635 UTC) and 260-min (after sunrise) (0900 UTC), for the rainfed and irrigated sites, respectively. This gives rise to a 150-min delay (0715 UTC) at the irrigated site compared with the rainfed site, during the thermal low regime. This demonstrates that a delay in the surface (2 m) buoyancy-flux generation over irrigated surfaces, relative to the arid rainfed surfaces, reduces the vertical intensity of turbulence during the morning transition period.

Figure 5 combines the vertical velocity variance from the tower heights with 30-min average profiles of vertical velocity variance (to a maximum height of 600 m) from the Halo Doppler lidar at the rainfed site. Five IOPs (IOP1-6) are presented when the Halo Doppler lidar was both operational and had good signal-to-noise ratios. There is good continuity between the vertical velocity variance from the eddy-covariance flux tower measurements and the remotely sensed vertical velocity variance from the Halo Doppler lidar. The vertical velocity variance threshold of 0.12 $m^2\ s^{-2}$ used in previous studies is not suitable for the Halo Doppler lidar dataset from the rainfed site, as the minimum vertical velocity variance is always greater than this threshold, including times when the boundary layer was stable. The criteria for defining convective onset was revised to 0.22 $m^2\ s^{-2}$ and combined with a skewness parameter greater than 0.1. The revised criteria for defining convective onset was determined by averaging the vertical velocity variance profiles at buoyancy flux crossover (and for the profiles either side of the buoyancy flux cross over time) for the five IOPs to determine the mean and standard deviation in the vertical velocity variance at crossover. The buoyancy flux crossover time was chosen as the important reference point in the morning transition period and occurring prior to convective onset. The vertical velocity variance at convective onset must exceed the vertical velocity variance at crossover. The profiles were averaged over the lowest 8 gates of the Doppler lidar (to a maximum of 240 m in height, although there was little sensitivity across the lowest 10 gates). The threshold of 0.22 $m^2\ s^{-2}$ exceeds the combined mean and standard deviation of the vertical velocity variance ($0.16\pm0.06\ m^2\ s^{-2}$).

The skewness parameter ($\overline{w'^3}/(\overline{w'^2})^{3/2}$) is the third-order moment of turbulence and is indicative of the asymmetry of the distribution of turbulence. Positive skewness represents narrow surface-driven updrafts. Vertical profiles of skewness are presented in Figure 5. The profiles combine with 30-min average skewness for the four tower heights. Again, there is reasonable continuity between the skewness calculated from the tower measurements and the Doppler lidar measurements, with closest agreement for the measurements at 25 m and 50 m.

Prior to convective onset, the variance profiles are uniform and neutral in shape and the skewness profiles show instrument noise fluctuating around zero. As the buoyancy flux begins to dominate, there is a marked shift in the magnitude of variance profiles and the shape of the profile begins to evolve. The profiles do not have a typical convective boundary layer variance profile shape but more representative of a mixed stable-convective state of the boundary layer, as has been seen in previous studies (Dunbar et al., 2013). Examples of these profiles include 06:45 UTC on 16

July and 19 July 2021. This mixed stable-convective state is indicative of the turbulent kinetic energy of the layer still dominated by shear. Figure 5 also presents the vertical velocity variance profile 30 minutes after convective onset (i.e. 0715 UTC for IOP1–4 and 0815 UTC for IOP7) and demonstrates a more typical convective boundary layer variance profile shape. The variance profiles for IOP4 (19 July) demonstrates a classical transition from stable state to mixed stable-convective state into an established convective boundary layer.

The times that convective onset is established at the rainfed site for different atmospheric heights (50, 120 and 200 m) is summarised in Table 5. The times of convective onset at 120 m and 200 m at the rainfed site for the five case studies examined show the propagation and vertical growth of turbulence through the morning transition between 50 m and 200 m generally occurs within the 30-min averaging window of the Doppler lidar data.

Equivalent vertical velocity variance profiles for the irrigated site are not available, and instead Figure 5 presents vertical profiles of turbulent kinetic energy (TKE) to a maximum height of 220 m from the Leosphere Windcube combined with 30-min average TKE for the three tower heights. TKE is an important measure of turbulence as it describes the vertical and horizontal mixing through the boundary layer. There is good overlap between the TKE calculated from the tower measurements and the Leosphere Windcube measurements when the TKE is small in the earliest part of the morning transition, although the overlap decreases later in the morning transition with larger TKE from the Leosphere Windcube compared with the tower measurements. An equivalent threshold for determining convective onset using the TKE data is not applied. The TKE profiles are also suggestive that the morning transition is delayed during the thermal heat low case (IOP6) compared with the synoptic westerly flow cases (IOP1–4), consistent with the analysis of vertical velocity variance. The delay to the morning transition during the thermal heat low case (IOP6) is explored further in section 3.5 where the strength of the near-surface inversion is examined for the three meteorological regimes.

## 3.4 | Boundary-layer structure: vertical wind profiles

Figure 6 presents the vertical wind profiles from radiosondes at the rainfed and irrigated site for the lowest 800 m. The comparisons are shown for the times closest to sunrise (0400 UTC) and convective onset. The vertical profile of wind direction is presented only at the time of sunrise. It is evident there is day-to-day variability in the structure of the vertical wind profiles, although within the three regimes there are consistencies between them. For example, the wind profiles for the synoptic scale westerly flow regime (IOP1–3) are relatively uniform in the lowest 600 m, with little variability in wind speed (3-5 m $s^{-1}$) throughout the morning transition period. The wind direction (0400 UTC) also shows little variability with height and is consistent between the two sites and highlights the dominance of the westerly synoptic scale flow.

There is greater variability in wind direction evident during IOP5–7, both in terms of vertical height and between the two sites, when the thermal low drives the flow regime. The irrigated site is influenced more predominately by easterly flow, whilst the rainfed site shows south-easterly to south-westerly variations. The low levels winds are seemingly disconnected between the two sites. Without the presence of synoptic scale westerly flow, local nocturnal flows are established, and the direction and strength of these winds are strongly influenced by local topography. This

is supported by the windrose analysis presented in Figure 1. At sunrise, a distinctive peak in the vertical profile of wind velocity, indicative of the nocturnal low-level jet (LLJ), is more prominent during the thermal low regime (IOP5–7). The mean height of the LLJ is 97±38 m. There is also no significant difference in the LLJ strength between the two sites, with the mean LLJ wind speed maximum of 5.8±1.1 m $s^{-1}$ and 4.8±0.9 m $s^{-1}$, for the rainfed and irrigated sites, respectively. At the rainfed site, there is an increase in the LLJ intensity between IOP5 and IOP7, from 4.5 to 7.2 m $s^{-1}$. All profiles show a slowing of the peak wind velocity at convective onset, as turbulent mixing increases driven by surface heating, and momentum in the low-level jet is mixed downwards. Table 1 summarises the LLJ during the thermal low regime (IOP5–7) in terms of the mean height and maximum wind speed.

The vertical wind profiles observed during this study support the findings of Cuxart et al. (2012) who investigated the within-basin dynamics for the eastern Ebro basin when boundary layer driven regimes are predominant, typically in anticyclonic conditions. Cuxart et al. (2012) showed nighttime downslope flows leading to the formation of a LLJ at a height near 200 m above the level of the basin bottom were routinely found.

The vertical profiles for the anticyclonic regime (IOP10) are distinctly different, with low wind velocity (< 2.0 m $s^{-1}$) in the lowest several hundred meters. This is evident at both site locations. At the rainfed site, wind speeds increase from 0.5 to 5.5 m $s^{-1}$ between 500 m and 700 m. At the irrigated site, wind speeds increase by a similar magnitude (0.5 to 6.8 m $s^{-1}$) but over a deeper layer (200 m to 700 m).

## 3.5 | Boundary-layer structure: potential temperature profiles

The end of the morning transition is defined as the time of convective onset at some height above the surface which should, in general, be equivalent to the depth of the majority of surface inversions observed under the region of interest. In section 3.3 we derived timings of convective onset based on eddy-covariance variance of vertical velocity 50 m, remote sensed vertical velocity variance and TKE at 200 m. In this section, we examine the structure and evolution of potential temperature profiles through the morning transition period, firstly using radiosonde profiles and secondly with a focus at the near-surface. The radiosonde profiles representing convective onset for IOP1 is 0600 UTC, IOP2–4 are at 0700 UTC, and IOP5–7&10 are at 0800 UTC. For consistency, the near-surface potential temperature profiles are for the same time as the radiosonde profiles.

Figure 7 presents the potential temperature profiles between 2 m and 800 m, at the irrigated and rainfed sites, focused on the times of sunrise and convective onset. The profiles at sunrise demonstrate the rainfed site has a tendency to form a more stable, shallow, surface layer (stable boundary layer). This difference is particularly pronounced during the thermal low (regime 2) and anticyclonic (regime 3) regimes. It is evident on all IOPs, colder temperatures are found at the irrigated site during the morning transition (also observed during the night) which extend through much of the boundary layer. The potential temperature profile at the irrigated site is colder than the corresponding profile at the rainfed site. The potential temperature profiles start cold, combined with larger evaporative cooling during the day (associated with an increased heat capacity due to the higher water content of the irrigated soil), which results in the cold temperature bias growing in magnitude through the morning transition period.

At both sites, the mixed layer profiles at convective onset are colder than the profiles at sunrise. It is important to

note the complex structure of the potential temperature profiles at both sites, with evidence of a number of residual layers above the convective boundary layer. The potential temperature profile at the rainfed site on IOP2 (16 July) demonstrates the residual layering very clearly; a 1.0 K inversion capping the convective boundary layer is seen at 480 m and above this two further residual layers are evident. This first is capped by a 0.6 K inversion at 600 m and the second is capped by a 0.7 K inversion at 730 m. The residual layer is indicative of the boundary layer structure from the previous day and may also be convolved with the impact of the surface heterogeneity for the region. However, it is not generally representative of the site location due to overnight advection.

The morning transition is strongly influenced by the wind profiles, as discussed in the previous section. The synoptic-scale westerly flow regime (IOP1–4) leads to a rapid transition from a stable boundary layer to an unstable boundary layer between the 06 UTC and 07 UTC sounding (not shown). At convective onset (regime 1), the average boundary layer depths are relatively consistent between the irrigated site (519±101m) and rainfed site (532±83m). In contrast, during the thermal low (regime 2) and anticyclonic (regime 3) regimes, the transition length from a stable boundary layer to an unstable boundary layer is more prolonged and differences in the boundary layer depth at convective onset are more pronounced. At convective onset, the average boundary layer depths (for regime 2 and 3) are deeper between the rainfed site (462±146m) compared with the irrigated site (208±64m). This is despite a stronger, shallower stable boundary layer at the rainfed site at sunrise. The boundary layer depths at convective onset for individual IOPs are summarised in Table 1.

Observations of the near-surface potential temperature from the 50 m tower were compared with the radiosonde profiles (not shown) and the analysis demonstrates good agreement, both at the time of sunrise and at convective onset. Figure 8 presents a focused analysis of the near-surface potential temperature profiles between 2 m and 50 m at the irrigated and rainfed sites, focused on the times of sunrise and convective onset. Table 6 summarises the magnitude of the temperature differences between the irrigated and rainfed sites (irrigated minus rainfed) with a focus on two levels on the flux tower; the screen level and the maximum tower height level. Noting, the screen level is $T_{2.0m}$ at the irrigated site and $T_{1.2m}$ at the rainfed site, and similarly the maximum height level is $T_{45m}$ at the irrigated site and $T_{50m}$ at the rainfed site. At sunrise, the average screen-level temperature difference (irrigated minus rainfed) is -1.2 K (range of -2.5 to 0.8 K). At the maximum height level ($T_{45m}$, $T_{50m}$) the temperature difference is -1.9 K (range of -0.6 to -4.4 K). This demonstrates the temperature differences between irrigated and rainfed sites are already present at the start of the morning transition and also supports the stronger stability for the rainfed stable boundary layer. At convective onset, the temperature differences between the two sites are accentuated with an average screen-level temperature difference of -3.6 K (range of -2.4 to -6.0 K) and -2.4 K (range of -0.9 to -4.3 K) at the maximum height level ($T_{45m}$, $T_{50m}$). The range presented across the IOPs shows there is considerable day-to-day variability in temperature contrasts at a regional level.

The average maximum daytime temperature ($T_{max}$) difference (irrigated minus rainfed) at screen level ($T_{2.0m}$, $T_{1.2m}$) is -2.8 K (range of -1.5 to -3.8 K). The $T_{max}$ differences are marginally smaller than the temperature differences at convective onset. The average $T_{max}$ difference for the maximum height level ($T_{45m}$, $T_{50m}$) is -0.5 K (range of -0.3 to -0.6 K). The temperature differences are smaller in magnitude than at either at sunrise or convective onset and the variability between meteorological regimes is reduced. The results from the LIAISE region are generally consistent with the tem-

perature contrasts at a regional scale from the literature; where suppression of the maximum daytime temperatures due to irrigation can locally be as large as −3.0 K to −8.0 K (Cook et al. 2015; Han and Yang 2013; Huber et al. 2014; Alter et al. 2015; Im et al. 2014). The results here emphasise that temperature contrasts are significant through the morning transition period and are largest in magnitude at convective onset (compared with $T_{max}$). This highlights the morning transition is a key part of the development of the convective boundary layer.

## 3.6 | Boundary-layer structure: specific humidity profiles

Figure 9 presents the near-surface specific humidity profiles through the morning transition at the irrigated and rainfed sites, again focused on the times of sunrise and convective onset. It is evident that for the morning transition period, distinctions between irrigated and rainfed surfaces, and between the meteorological regimes, are not as clearly defined as was seen for the kinematic buoyancy flux, vertical profiles of turbulence or the vertical profiles of potential temperature. This highlights the complexity of understanding boundary layer humidity evolution, especially considering the large differences in surface moisture fluxes at the two sites.

For two of the westerly flow regime IOPs (IOP1&4) the near-surface specific humidity profiles are very similar for the rainfed and irrigated sites. There are no discernible differences in the humidity profiles between the start and end of the morning transition period. In contrast, for the thermal low regime (IOP5–7), the specific humidity profiles at the irrigated site are moister than at the rainfed site. At convective onset, the specific humidity differences between the two sites increase on each consecutive day from 1.3 g kg$^{-1}$ (IOP5) to 1.9 g kg$^{-1}$ (IOP6) to 4.7 g kg$^{-1}$ (IOP7). In general, at the irrigated site there is virtually no gradient in specific humidity between 10 m and 50 m, at sunrise or convective onset, on any of the IOPs. The gradients are most prominent between 0.2 m and 2 m. The largest gradients between 0.2 m and 2 m are seen towards the end of the morning transition on IOP7 (22 July) and IOP10 (27 July) with differences of 2.2 g kg$^{-1}$ and 3.0 g kg$^{-1}$, respectively.

IOP2 (16 July) is an unusual case, as the specific humidity at the rainfed is greater than the irrigated site. This is the only IOP where this is observed. At the start of the morning transition (04 UTC), the specific humidity at 10 m is 10.8 kg$^{-1}$ and 9.0 kg$^{-1}$ at the rainfed and irrigated sites, respectively. At the rainfed site, the specific humidity at 10 m (50 m) decreases by 2.7 g kg$^{-1}$ (1.2 g kg$^{-1}$) during the morning transition in contrast to the irrigated site which dries by 0.6 g kg$^{-1}$ (0.2 g kg$^{-1}$). At the rainfed site, examining the specific humidity gradient between 10 m and 50 m suggests dry advection occurs between 0345 UTC and 0445 UTC corresponding to a wind veering from westerly at 0345 UTC to south-westerly (drier) at 0445 UTC. A westerly wind has a fetch over irrigated surfaces, whilst a southerly wind has a fetch over an arid surface for a significant distance. The wind transitions back to westerly flow at 0515 UTC but no further changes in the specific humidity are observed.

As the diurnal cycle progresses (plot not shown) differences in specific humidity (irrigated minus rainfed) increase in magnitude. The mean specific humidity difference at 2 m (for 1400–1600 UTC) was 3.0 g kg$^{-1}$ moister during the synoptic-scale westerly flow regime (IOP1–4) and 4.6 g kg$^{-1}$ moister during the thermal low regime (IOP5–7) and anticyclonic regime (IOP10) at the irrigated site compared with the rainfed site. The specific humidity time series (not shown) highlights that significant drying occurs throughout the afternoon at the rainfed site, whilst the surface

moisture flux (latent heat flux) acts to maintain or increase the surface specific humidity at the irrigated site leading to a growing difference in specific humidity between the two sites. More generally however, this does suggest that there are processes acting overnight (occurring between the evening transition and morning transition periods) to homogenise the humidity differences between the rainfed and irrigated regions. Understanding these mechanisms must be left for future work.

The increase in soil moisture from irrigation processes has been directly shown to modulate near-surface humidity in other observational studies. Results from the GRAINEX campaign in the Great Plains (Nebraska, US) have shown near-surface humidity profiles are 2.0 g $kg^{-1}$ moister for irrigated surfaces (Rappin et al., 2021). These differences reported for GRAINEX are somewhat smaller compared with LIAISE and this is largely due to the different climates for the study regions; humid continental type of climate (Köppen climate classification Dfa) for GRAINEX compared with semi-arid climate (Köppen climate classification Bsk) for LIAISE.

## 4 | CONCLUSIONS

The Land surface Interactions with the Atmosphere over the Iberian Semi-arid Environment (LIAISE) campaign was conducted in the summer of 2021 to investigate the role of irrigation in modulating the boundary layer evolution in the Urgell and Pla d'Urgell in the Catalan region of northeastern Spain. Field observations over irrigated surfaces are essential to understand perturbations of near-surface meteorology, surface interactions with the boundary layer, for developing and testing irrigation schemes and for evaluating their performance. The campaign deployed a network of eddy-covariance flux sites across an important European food production region which has a significant irrigation presence surrounded by a rainfed region, which is arid during the summer months.

This study focused on observations at two supersites, one located in a rainfed (arid) zone and the other located in an irrigated zone. Intensive Observing Periods were achieved on eleven days with seven IOP days having simultaneous radio-soundings at the rainfed (arid) and irrigated sites with hourly launches. High temporal resolution hourly soundings were a priority for IOPs to observe the evolution of the boundary-layer thermodynamic profiles. LIAISE is the first of this type of field campaign in Europe and provides a unique observational dataset for investigating the role of irrigation in modulating the boundary layer evolution. This study examined the impact of irrigation on the morning transition period, a crucial part of the diurnal cycle for the developing convective boundary layer, but one that is frequently overlooked.

The results of this study have demonstrated a local redistribution of near-surface heat, water and energy arising from the presence of irrigation which modulates the vertical gradients of turbulence, temperature, and moisture. The results have emphasised that contrasts arising from irrigation are significant through the morning transition period, and have highlighted that the morning transition is a key part of the development of the convective boundary layer.

Surface observations showed significant contrasts between the irrigated and rainfed (arid) sites. Evapotranspiration was observed to dominate the flux partitioning at the irrigated site, whilst sensible heat flux dominated at the rainfed (arid) site. The cumulative evapotranspiration during July 2021 at the irrigated site was a factor of 10 greater (69.9 kg $m^{-2}$) than at the rainfed (arid) site (5.6 kg $m^{-2}$). The Bowen ratio was in the range of 0.07–1.1 at the irrigated

site compared with greater than 10.0 at the rainfed (arid) site. Irrigation was shown to suppress the near-surface turbulence generation during the morning transition period. The morning transition mean surface buoyancy flux was 2.8 times smaller at the irrigated site (1.1 $m^2\ s^{-2}$) than at the rainfed (arid) site (3.1 $m^2\ s^{-2}$). The vertical intensity of turbulence at 50 m was smaller over irrigated surfaces compared with over rainfed surfaces.

Colder near-surface temperatures were found at the irrigated site relative to the rainfed (arid) site. This was combined with a less stable, deeper, surface layer (stable boundary layer) at the irrigated site. These temperature differences (irrigated minus rainfed) were observed at the start of the morning transition (sunrise) and the differences between the sites increased in magnitude throughout the morning transition period. The colder temperatures at sunrise at the irrigated site are predominately the result of colder boundary layer thermodynamic profile from the previous day. At the start of the morning transition (sunrise), the average screen-level (50 m) temperature difference was -1.2 K (-1.9 K) between the irrigated and rainfed (arid) sites.

By convective onset the temperature differences between the two sites extend through much of the boundary layer and increased in magnitude. Over irrigated surfaces there is larger evaporative cooling effect on the net surface heating during the day associated with an increased heat capacity due to the higher water content of the irrigated soil. In addition, the delay in the sensible heat flux becoming positive at the irrigated site leads to a generally smaller sensible heat flux during the morning transition period. At convective onset, the temperature differences between the two sites were shown to be accentuated with an average screen-level temperature difference of -3.6 K. By comparison, the average $T_{max}$ difference at screen level was found to be -2.8 K. This emphasises that temperature contrasts grow significantly through the morning transition period and are larger in magnitude at convective onset compared with the maximum daytime temperature ($T_{max}$).

The morning transition was shown to be strongly influenced by the wind profiles. At convective onset, differences in the boundary layer depth at the two sites were pronounced during the thermal low and anticyclonic regimes. The average boundary layer depths was found to be deeper between the rainfed site (462±146m) compared with the irrigated site (208±64m). During the synoptic-scale westerly flow regime a rapid transition from a stable boundary layer to an unstable boundary layer occurred and the average boundary layer depth were found to be relatively consistent between the irrigated site (519±101m) and rainfed site (532±83m).

This study has demonstrated some variability in near-surface specific humidity during the morning transition period on individual IOP days, although significant differences between irrigated and rainfed surfaces, and between the meteorological regimes were not as clearly defined as with the many other parameters discussed in this paper. This particularly highlights the complexity of understanding boundary layer humidity evolution, especially considering the large differences in surface moisture fluxes at the two sites. The mean daytime (1400–1600 UTC) specific humidity (at 2 m) was greater at the irrigated site compared with the rainfed (arid) site, on the order of 3.0 g $kg^{-1}$ for the synoptic scale westerly flow regime (IOP1–4) and 4.6 g $kg^{-1}$ for the thermal low and anticyclonic regimes (IOP5–7&10).

It is evident from the observations presented in this study that weather and climate models which do not represent irrigated processes will incorrectly represent soil moisture, leading to incorrect heat and moisture flux partitioning at the surface, impacting on the heat and moisture turbulent fluxes through the boundary layer. This will lead to significant errors in key forecast diagnostics that are used for model verification including screen-level temperature,

land-surface (skin) temperature, humidity and wind speed.

In conclusion, this study has demonstrated that contrasts arising from irrigation are significant through the morning transition period and are well established at convective onset. Observations from LIAISE will be used to further study how the convective boundary layer develops throughout the daytime period and will be used to explore the impacts of surface-flux contrasts. For example the modification of regional winds within and downwind of irrigated areas leading to the generation of secondary circulations as well as the modulation of heat and moisture non-local advection processes.

**TABLE 1** Summary of LIAISE Intensive Observation Periods discussed within this study. The summary states times of radiosonde launches, wind characteristics including low-level jet (0400 UTC) (for IOP5–7), boundary layer depth (at convective onset) and sea breeze duration at the irrigated and rainfed site. The meteorological conditions for each IOP are stated.

| IOP | Date | Radio soundings | | Low-level jet (0400 UTC) | | Boundary Layer Depth (Onset) | | Sea breeze duration | | Meteorological |
|---|---|---|---|---|---|---|---|---|---|---|
| | | Irrigated [UTC] | Rainfed [UTC] | Irrigated [m $s^{-1}$] | Rainfed [m $s^{-1}$] | Irrigated [m] | Rainfed [m] | Irrigated [UTC] | Rainfed [UTC] | Conditions |
| IOP1 | 15 July | 06, 08–17 | 04–17 | - | - | 662 | 649 | 1945–2115 | 1915–2245 | Clear-sky, westerly flow |
| IOP2 | 16 July | 04–17 | 04–21 | - | - | 434 | 488 | 1915–2045 | 1915–2245 | Clear-sky, westerly flow |
| IOP3 | 17 July | 04–17 | 04–17 | - | - | 463 | 459 | 1900–2020 | 1750–2145 | Clear-sky, westerly flow |
| IOP4 | 19 July | 04–17 | - | - | - | 436 | - | 1800–2030 | 1615–2140 | Clear-sky, westerly flow |
| IOP5 | 20 July | 04–17 | 04–17 | 5.6 (70 m) | 4.5 (71 m) | 307 | 661 | 1410–1845 | 1145–1900 | Clear-sky, thermal low |
| IOP6 | 21 July | 04–17 | 04–17, 19, 21 | 3.5 (165 m) | 5.7 (130 m) | 220 | 293 | 1600–1900 | 1400–2000 | Clear-sky, thermal low |
| IOP7 | 22 July | 04–17 | 04–17, 19–21 | 5.5 (70 m) | 7.2 (74 m) | 134 | 541 | 1540–2325 | 1245–1920 | Clear-sky, thermal low |
| IOP10 | 27 July | 04–17, 21 | 04–21 | - | - | 171 | 354 | 1610–1935 | 1415–2150 | Clear-sky, anticyclonic |

**TABLE 2** Times of the morning buoyancy-flux crossover relative to the time of sunrise at different heights from the tower measurements during Intensive Observation Periods. N.B crossover times for all rainfed heights and irrigated at 2 m is derived from 10-min data, whilst crossover times for irrigated at 3, 25 and 50 m is derived from 30-min data.

| IOP | Date | Sunrise | Buoyancy-flux crossover time | | | | | | | |
|---|---|---|---|---|---|---|---|---|---|---|
| | | | Irrigated | | | | Rainfed | | | |
| | | | 2 m | 3 m | 25 m | 50 m | 2 m | 10 m | 25 m | 50 m |
| | | [UTC] | [min] | [min] | [min] | [min] | [min] | [min] | [min] | [min] |
| IOP1 | 15 July | 0443 | - | +62 | +92 | +122 | +52 | +52 | +52 | +62 |
| IOP2 | 16 July | 0444 | +96 | +91 | +91 | +91 | +61 | +61 | +81 | +81 |
| IOP3 | 17 July | 0445 | +85 | +60 | +120 | +120 | +60 | +60 | +70 | +80 |
| IOP4 | 19 July | 0446 | +74 | +59 | +119 | +149 | +49 | +69 | +69 | +79 |
| IOP5 | 20 July | 0447 | +173 | +118 | +118 | +148 | +68 | +78 | +78 | +88 |
| IOP6 | 21 July | 0448 | +182 | +87 | +147 | +177 | +57 | +87 | +97 | +97 |
| IOP7 | 22 July | 0449 | +251 | +206 | +146 | +176 | +56 | +86 | +116 | +126 |
| IOP10 | 27 July | 0454 | +86 | +81 | +111 | +141 | +61 | +91 | +91 | +101 |

**TABLE 3** The morning transition mean buoyancy flux and latent heat flux contribution to the buoyancy flux for the morning transition period for the irrigated and rainfed sites during Intensive Observation Periods. The morning transition is defined as 04–06 UTC for IOP1, 04–07 UTC for IOP2–4, and 04–08 UTC for IOP5–10.

| IOP | Date | Mean buoyancy-flux | | Latent heat flux contribution to buoyancy-flux | | | | | | | |
|---|---|---|---|---|---|---|---|---|---|---|---|
| | | Irrigated | Rainfed | Irrigated | | | | Rainfed | | | |
| | | 2 m | 2 m | 2 m | 3 m | 25 m | 50 m | 2 m | 10 m | 25 m | 50 m |
| | | [$10^3$ m$^2$ s$^{-3}$] | [$10^3$ m$^2$ s$^{-3}$] | [%] | [%] | [%] | [%] | [%] | [%] | [%] | [%] |
| IOP1 | 15 July | 2.1 | 3.8 | 13.3 | 11.4 | 10.7 | 19.3 | 0.3 | 0.4 | 0.3 | 0.4 |
| IOP2 | 16 July | 1.1 | 3.2 | 20.1 | 13.8 | 13.6 | 17.8 | 0.7 | 1.2 | 1.3 | 1.3 |
| IOP3 | 17 July | 0.9 | 3.1 | 24.4 | 13.4 | 16.8 | 20.8 | 0.8 | 1.3 | 1.3 | 1.3 |
| IOP4 | 19 July | 0.8 | 3.0 | 29.2 | 25.0 | 11.0 | 23.0 | 0.3 | 0.1 | 0.1 | 0.1 |
| IOP5 | 20 July | 0.9 | 2.1 | 41.3 | 37.0 | 28.7 | 25.2 | 1.0 | 4.7 | 5.4 | 6.2 |
| IOP6 | 21 July | 0.3 | 2.0 | 89.6 | 89.9 | 58.1 | 42.4 | 5.3 | 8.3 | 10.1 | 0.0 |
| IOP7 | 22 July | - | 3.7 | - | 96.9 | 57.1 | 83.0 | 0.7 | 0.9 | 0.9 | 1.0 |
| IOP10 | 27 July | 1.4 | 4.1 | 36.4 | 37.4 | 24.3 | 35.7 | 1.9 | 1.7 | 2.1 | 2.2 |

**TABLE 4** The daytime mean (1000–1400 UTC) buoyancy flux and latent heat flux contribution to the buoyancy flux for the irrigated and rainfed sites during Intensive Observation Periods.

| IOP | Date | Daytime mean buoyancy-flux | | Latent heat flux contribution to buoyancy-flux | | | | | | | |
|---|---|---|---|---|---|---|---|---|---|---|---|
| | | Irrigated | Rainfed | Irrigated | | | | Rainfed | | | |
| | | 2 m | 2 m | 2 m | 3 m | 25 m | 50 m | 2 m | 10 m | 25 m | 50 m |
| | | [$10^3$ m$^2$ s$^{-3}$] | [$10^3$ m$^2$ s$^{-3}$] | [%] | [%] | [%] | [%] | [%] | [%] | [%] | [%] |
| IOP1 | 15 July | 5.1 | 10.6 | 12.5 | 8.5 | 9.0 | 10.4 | 0.1 | 0.0 | 0.0 | 0.0 |
| IOP2 | 16 July | 4.5 | 10.4 | 17.5 | 10.5 | 11.0 | 13.0 | 0.3 | 0.6 | 0.6 | 0.7 |
| IOP3 | 17 July | 3.4 | 9.5 | 24.8 | 16.5 | 16.5 | 13.3 | 0.2 | 0.0 | 0.0 | 0.0 |
| IOP4 | 19 July | 2.6 | 9.5 | 39.7 | 19.9 | 16.3 | 19.9 | 0.2 | 0.0 | 0.0 | 0.0 |
| IOP5 | 20 July | 1.5 | 8.9 | 65.6 | 34.0 | 31.3 | 46.7 | 0.0 | 0.2 | 0.3 | 0.3 |
| IOP6 | 21 July | 1.7 | 9.0 | 77.7 | 48.8 | 34.1 | 43.9 | 0.6 | 0.5 | 0.5 | 0.5 |
| IOP7 | 22 July | 1.3 | 8.9 | - | 62.2 | 47.5 | 91.6 | 0.2 | - | - | - |
| IOP10 | 27 July | 2.0 | 9.1 | 54.5 | 56.9 | 40.9 | 46.4 | 0.8 | - | - | - |

**TABLE 5** Times of convective onset (based on 30-min average data) relative to the time of sunrise during Intensive Observation Periods. Times of convective onset at 50 m are based on eddy-covariance vertical velocity variance measurements at the irrigated and rainfed sites. Times of convective onset at 120 m and 200 m at the rainfed site are based on Doppler lidar vertical velocity variance and skewness measurements.

| IOP | Date | Sunrise [UTC] | Irrigated [min] | Rainfed [min] | | |
|---|---|---|---|---|---|---|
| | | | 50 m | 50 m | 120 m | 200 m |
| IOP1 | 15 July | 0443 | +152 | +92 | +92 | +92 |
| IOP2 | 16 July | 0444 | +121 | +121 | +121 | +121 |
| IOP3 | 17 July | 0445 | +120 | +90 | +120 | +120 |
| IOP4 | 19 July | 0446 | +149 | +89 | +119 | +119 |
| IOP5 | 20 July | 0447 | +268 | +118 | - | - |
| IOP6 | 21 July | 0448 | +327 | +147 | +147 | +177 |
| IOP7 | 22 July | 0449 | +236 | +146 | - | - |
| IOP10 | 27 July | 0454 | +201 | +141 | - | - |

**TABLE 6** Temperature differences between the irrigated and rainfed sites (irrigated minus rainfed) at times of sunrise, convective onset, and maximum daytime temperature ($T_{max}$) during Intensive Observation Periods. Temperature differences are compared at two levels on the flux tower; the screen level ($T_{2.0m}$, $T_{1.2m}$) and maximum height level ($T_{45m}$, $T_{50m}$).

| IOP | Date | Irrigated - Rainfed $T_{2.0m}$, $T_{1.2m}$ [K] | | | Irrigated - Rainfed $T_{45m}$, $T_{50m}$ [K] | | |
|---|---|---|---|---|---|---|---|
| | | Sunrise | Convective Onset | $T_{max}$ | Sunrise | Convective Onset | $T_{max}$ |
| IOP1 | 15 July | -1.1 | -2.4 | -1.5 | -0.6 | -0.9 | -0.5 |
| IOP2 | 16 July | 0.8 | -2.4 | -2.1 | -0.9 | -1.6 | -0.6 |
| IOP3 | 17 July | -1.7 | -3.0 | -2.4 | -1.3 | -2.0 | -0.6 |
| IOP4 | 19 July | -1.3 | -3.4 | -2.5 | -1.2 | -2.3 | -0.5 |
| IOP5 | 20 July | -2.3 | -4.0 | -3.0 | -1.3 | -2.3 | -0.2 |
| IOP6 | 21 July | -2.5 | -3.9 | -3.6 | -4.4 | -2.5 | -0.5 |
| IOP7 | 22 July | -0.4 | -6.0 | -3.8 | -1.6 | -4.3 | -0.6 |
| IOP10 | 27 July | -0.8 | -3.4 | -3.6 | -3.5 | -2.9 | -0.3 |
| Average | - | -1.2 | -3.6 | -2.8 | -1.9 | -2.4 | -0.5 |

## Data Availability

LIAISE campaign data is available through the LIAISE database maintained by the Data and Services for the Atmosphere (AERIS) (https://liaise.aeris-data.fr/page-catalogue). Data from the rainfed site (Els Plans) is available from Price (2023e,a,b,c,d). Data from the irrigated site (La Cendrosa) is available from Canut (2022a,b); Garrouste and Canut (2022).

## Acknowledgements

The authors would like to thank all of organizers, hosts and participants of the LIAISE campaign. The acquisition of part of the observations used in this study were funded by the French ANR-HILIAISE. The authors thank the support staff at the Met Office observations field site. We would like to acknowledge Joaquim Bellvert, Jan Polcher, Josep Ramon Miró and Pere Quintana for their work on the LIAISE steering committee. The authors thank Clare Bysouth for support with the VerPy Python library for handling verification data. The contribution of author J. K. Brooke was conducted through the Weather and Climate Science for Service Partnership (WCSSP) India, a collaborative initiative between the Met Office, supported by the UK Government's Newton Fund, and the Indian Ministry of Earth Sciences (MoES). Three anonymous reviewers are thanked for comments leading to improvements in the manuscript.

## References

Angevine, W., Baltink, H. and Bosveld, F. (2001) Observations of the morning transition of the convective boundary layer. *Boundary-Layer Meteorol.*, **101**, 209–227.

Angevine, W., Edwards, J., Lothon, M., LeMone, M. and Osborne, S. (2020) Transition periods in the diurnally-varying atmospheric boundary layer over land. *Boundary-Layer Meteorol.*, **177**, 205–223.

Arneth, A., Denton, F., Agus, F., Elbehri, A., Erb, K., Osman Elasha, B., Rahimi, M., Rounsevell, M., Spence, A. and Valentini, R. (2019) Framing and context. in: Climate change and land: an ipcc special report on climate change, desertification, land degradation, sustainable land management, food security, and greenhouse gas fluxes in terrestrial ecosystems. *IPCC*.

Barton, E. J., Taylor, C. M., Mitra, A. K. and Jayakumar, A. (2023) Systematic daytime increases in atmospheric biases linked to dry soils in irrigated areas in indian operational forecasts. *Atmospheric Science Letters*, **n/a**, e1172.

Barton, E. J., Taylor, C. M., Parker, D. J., Turner, A. G., Belušić, D., Böing, S. J., Brooke, J. K., Harlow, R. C., Harris, P. P., Hunt, K., Jayakumar, A. and Mitra, A. K. (2019) A case-study of land–atmosphere coupling during monsoon onset in northern india. *Quarterly Journal of the Royal Meteorological Society*, **146**, 2891–2905.

Lone, A., Best, M., Cuxart, J., Polcher, J., Quintana Seguí, P., Bellvert, J., Brooke, J., Canut-Rocafort, G. and Price, J. (2021) Updates on the international land surface interactions with the atmosphere over the iberian semi-arid environment (liaise) field campaign. *GEWEX News*, **31(4)**, 17–21.

Brooke, J. and Osborne, S. (2021) Observations and numerical weather forecasts of land-surface and boundary-layer evolution during an unusually dry spring at a site in central england. *Q.J.R. Meteorol. Soc.*, **148**, 15–34.

Canut, G. (2022a) LIAISE LA CENDROSA CNRM LIDARwindcube TKE L2. Aeris, https://doi.org/10.25326/321.

— (2022b) LIAISE LA CENDROSA CNRM MTO FLUX 30MIN L2. Aeris, https://doi.org/10.25326/320.

Chen, L. and Dirmeyer, P. (2020) Distinct impacts of land use and land management on summer temperatures. *Frontiers in Earth Science*, **8**.

Cook, B. I., Puma, M. J. and Krakauer, N. Y. (2011) Irrigation induced surface cooling in the context of modern and increased greenhouse gas forcing. *CLIMATE DYNAMICS*, **37**, 1587–1600.

Cuxart, J., Conangla, L. and Jiménez, M. A. (2015) Evaluation of the surface energy budget equation with experimental data and the ecmwf model in the ebro valley. *Journal of Geophysical Research: Atmospheres*, **120**, 1008–1022. URL: `https://agupubs.onlinelibrary.wiley.com/doi/abs/10.1002/2014JD022296`.

Cuxart, J., Cunillera, J., Jiménez, M. A., Martínez, D., Molinos, F. and Palau, J. L. (2012) Study of mesobeta basin flows by remote sensing. *Boundary-Layer Meteorology*, **143**, 143–158.

Dunbar, T., Barlow, J. and Belcher, S. E. (2013) An optimal inverse method using doppler lidar measurements to estimate the surface sensible heat flux. *Boundary-Layer Meteorology*, **150**.

Garrouste, O. and Canut, G. (2022) LIAISE LA CENDROSA CNRM RS L. Aeris, https://doi.org/10.25326/322.

Hogan, R., Grant, A., Illingworth, A., Pearson, G. and O'Connor, E. (2009) Vertical velocity variance and skewness in clear and cloud-topped boundary layers as revealed by doppler lidar. *Quart. J. Royal Meteorol. Soc.*, **135**, 635–643.

Jia, G., Shevliakova, E., Artaxo, P., Noblet-Ducoudré, N. D., Houghton, R., House, J., Kitajima, K., Lennard, C., Popp, A., Sirin, A., Sukumar, R. and Verchot, L. (2019) Land–climate interactions. in: Climate change and land: an IPCC special report on climate change, desertification, land degradation, sustainable land management, food security, and greenhouse gas fluxes in terrestrial ecosystems. *IPCC*.

Lanicci, J. M., Carlson, T. N. and Warner, T. T. (1987) Sensitivity of the great plains severe-storm environment to soil-moisture distribution. *Monthly Weather Review*, **115**, 2660 – 2673.

Lawston, P., Santanello, J., Hanson, B. and Arsensault, K. (2020) Impacts of irrigation on summertime temperatures in the pacific northwest. *Earth Interactions*, **24**, 1–26.

Lawston, P. M., Santanello, J. A., Zaitchik, B. F. and Rodell, M. (2015) Impact of irrigation methods on land surface model spinup and initialization of wrf forecasts. *Journal of Hydrometeorology*, **16**, 1135 – 1154. URL: `https://journals.ametsoc.org/view/journals/hydr/16/3/jhm-d-14-0203_1.xml`.

Legain, D., Bousquet, O., Douffet, T., Tzanos, D., Moulin, E., Barrie, J. and Renard, J.-B. (2013) High-frequency boundary layer profiling with reusable radiosondes. *Atmospheric Measurement Techniques*, **6**, 2195–2205.

Lobell, D. B., Bala, G., Bonfils, C. and Duffy, P. B. (2006) Potential bias of model projected greenhouse warming in irrigated regions. *Geophysical Research Letters*, **33**.

Mangan, M., Hartogensis, O., Boone, A., Branch, O., Canut, G., Cuxart, J., de Boer, H., Le Page, M., Martínez-Villagrasa, D., Miró, J., Price, J. and Vilà-Guerau de Arellano, J. (2023) The surface-boundary layer connection across spatial scales of irrigation-driven thermal heterogeneity: An integrated data and modeling study of the liaise field campaign. *Agricultural and Forest Meteorology*, **335**.

Pearson, G., Davies, F. and Collier, C. (2009) An analysis of the performance of the ufam pulsed doppler lidar for observing the boundary layer. *J. Atmos. Oceanic Technol.*, **26**, 240–250.

Price, J. (2023a) LIAISE ELS PLANS UKMO Doppler Lidar Stare L1. Aeris, https://doi.org/10.25326/436.

— (2023b) LIAISE ELS PLANS UKMO Doppler Lidar Wind Profile L1. Aeris, https://doi.org/10.25326/434.

— (2023c) LIAISE ELS PLANS UKMO MTO 10MIN L2. Aeris, https://doi.org/10.25326/43.

— (2023d) LIAISE ELS PLANS UKMO MTO 30MIN L2. Aeris, https://doi.org/10.25326/430.

— (2023e) LIAISE ELS PLANS UKMO radiosondes L1. Aeris, https://doi.org/10.25326/429.

Rappin, E., Mahmood, R., Nair, U., Pielke, R. A., Brown, W., Oncley, S., Wurman, J., Kosiba, K., Kaulfus, A., Phillips, C., Lachenmeier, E., Santanello, J., Kim, E. and Lawston-Parker, P. (2021) The great plains irrigation experiment (grainex). *Bulletin of the American Meteorological Society*, **102**, E1756–E1785.

Reen, B., Stauffer, D. and Davis, K. (2014) Land-surface heterogeneity effects in the planetary boundary layer. *Boundary-Layer Meteorol*, **150**, 1–31.

Shukla, P., Skea, J., Slade, R., van Diemen, R., Haughey, E., Malley, J., Pathak, M. and Pereira, J. P. (2019) Technical summary, 2019. in: Climate change and land: an ipcc special report on climate change, desertification, land degradation, sustainable land management, food security, and greenhouse gas fluxes in terrestrial ecosystems. *IPCC*.

Trooshian, S., Li, J., Hsu, K.-l. and Gao, X. (2011) How significant is the impact of irrigation on the local hydroclimate in california's central valley? comparison of model results with ground and remote-sensing data. *Journal of Geophysical Research: Atmospheres*, **116**.

Thiery, W., Visser, A. and Fischer, E. (2020) Warming of hot extremes alleviated by expanding irrigation. *Nat Commun*, **11**, 290.

Valmassoi, A. and Keller, J. D. (2022) A review on irrigation parameterizations in earth system models. *Frontiers in Water*, **4**.

de Vrese, P. and Hagemann, S. (2018) Uncertainties in modelling the climate impact of irrigation. *Clim Dyn*, **51**, 2023–2038.

Xia, Q., Liu, P., Fan, Y., Cheng, L., An, R., Xie, K. and Zhou, L. (2022) Representing irrigation processes in the land surface-hydrological model and a case study in the yangtze river basin, china. *Journal of Advances in Modeling Earth Systems*, **14**.

Zaveri, E. B. and Lobell, D. (2019) The role of irrigation in changing wheat yields and heat sensitivity in india. *Nat Commun*, **10**, 4144.

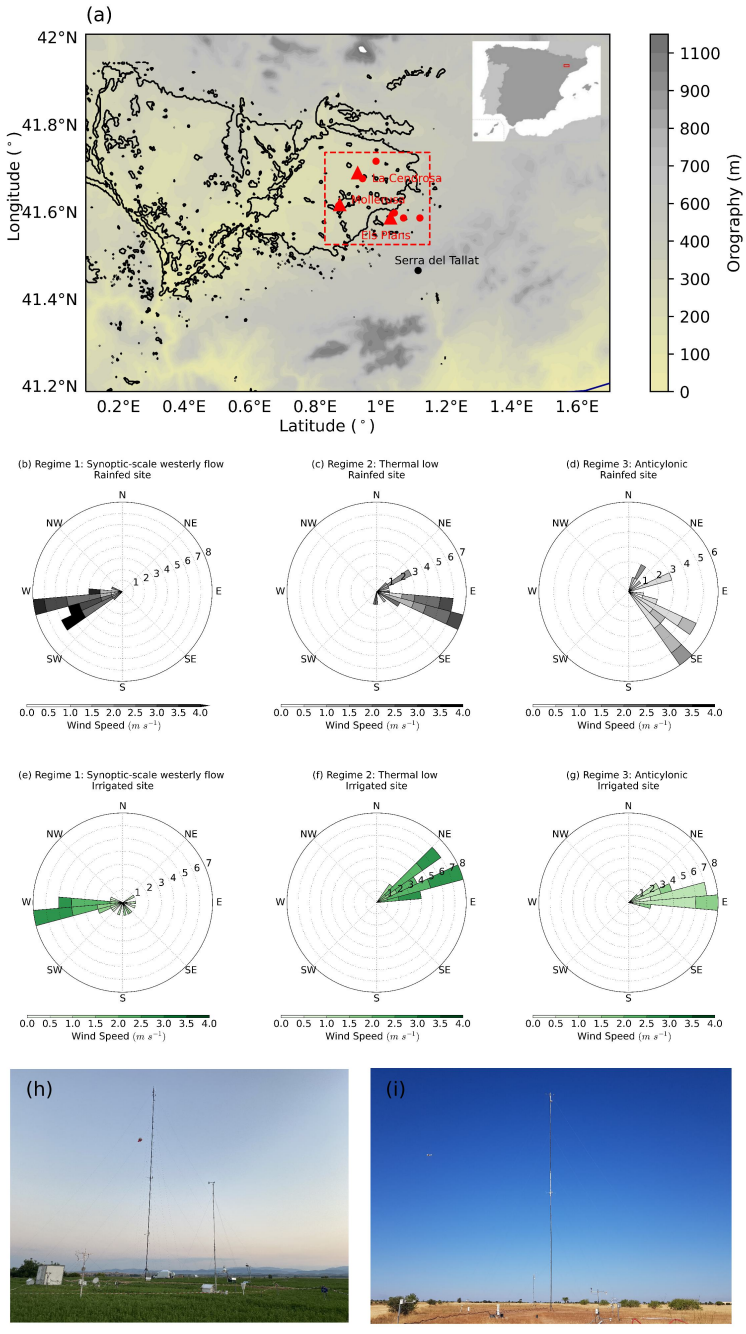


**FIGURE 1** (a) Map of the LIAISE study region including (red triangles) Els Plans and La Cendrosa supersite locations, (red dots) eddy-covariance flux site locations and (black line) the irrigated region from the ESA Climate Change Initiative Land Cover (ESA CCI LC) dataset. Also presented is the topographic data from the Global Multi-resolution Terrain Elevation Data 2010 (GMTED2010) dataset. Windrose plots showing 2 m wind direction and speed during the morning transition at the rainfed site during three meteorological regimes (b) synoptic-scale westerly flow, (c) thermal low, and (d) anticyclonic. Windrose plots (e), (f) and (g) showing the same three meteorological regimes for the irrigated site. The radial axis on each windrose represents the number of observations in each wind direction. Photos of the (h) irrigated and (i) rainfed sites with the 50 m flux tower installations taken during the SOP in July 2021.

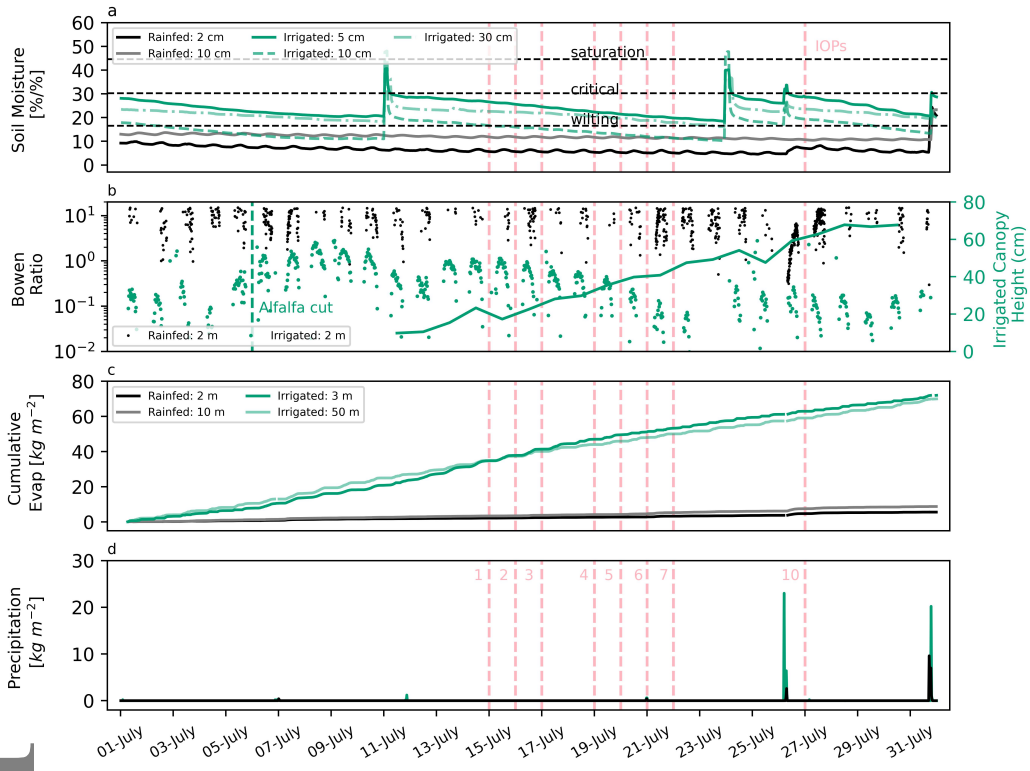


**FIGURE 2** Evolution during July 2021 of (a) volumetric soil moisture content, (b) Bowen ratio (observations at 2 m height), (c) cumulative evapotranspiration (observations at 2 m and 10 m height), and (d) precipitation, contrasting the rainfed site (Els Plans, black) and irrigated site (La Cendrosa, green). Panel a includes the soil saturation, wilting and critical points determined from the HWSD. Panel b highlights the date the alfalfa is cut. Panel d highlights the dates of the Intensive Observation Periods.

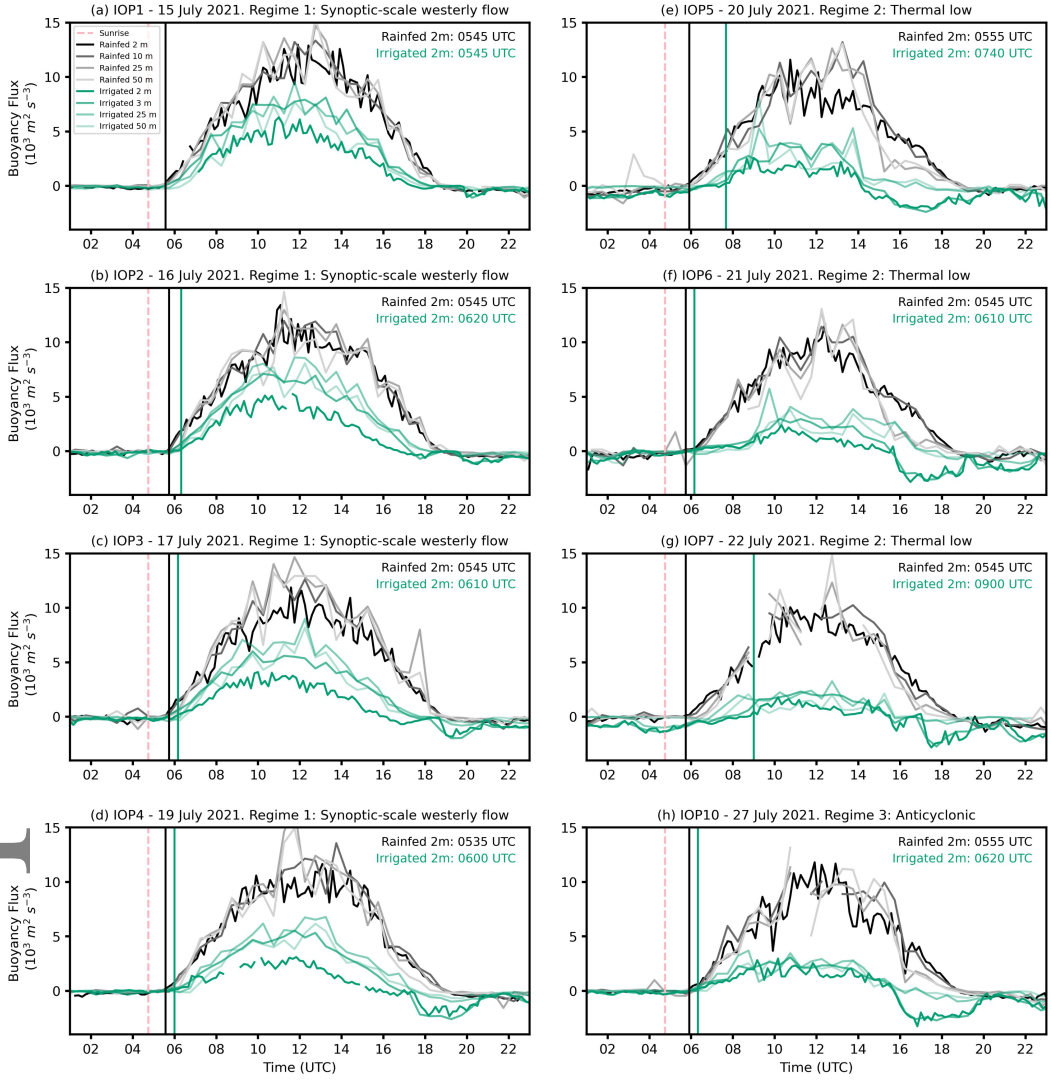


**FIGURE 3** Observed diurnal cycle of buoyancy flux on clear-sky IOP days contrasting the rainfed site (Els Plans, black) and irrigated site (La Cendrosa, green). Vertical lines indicate the time of sunrise (dashed line) and buoyancy-flux crossover time defined by a change in the sign of the buoyancy-flux observations at the two sites.

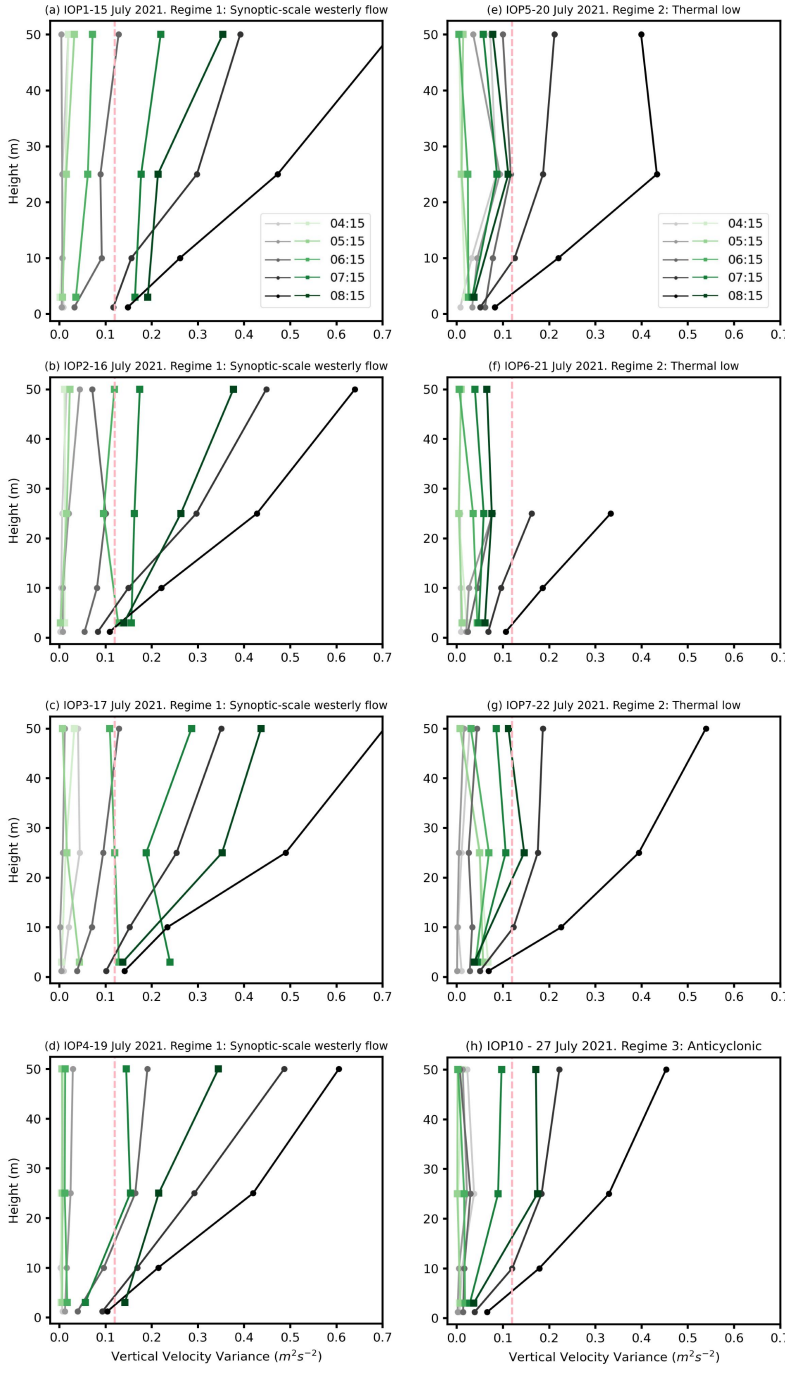


**FIGURE 4** Observed vertical velocity variance profiles from 2 m to 50 m on clear-sky IOP days contrasting the rainfed site (Els Plans, black) and irrigated site (La Cendrosa, green). The vertical dashed line indicates the 0.12 $m^2$ $s^{-2}$ threshold from Hogan et al. (2009) which is applied to indicate convective onset.

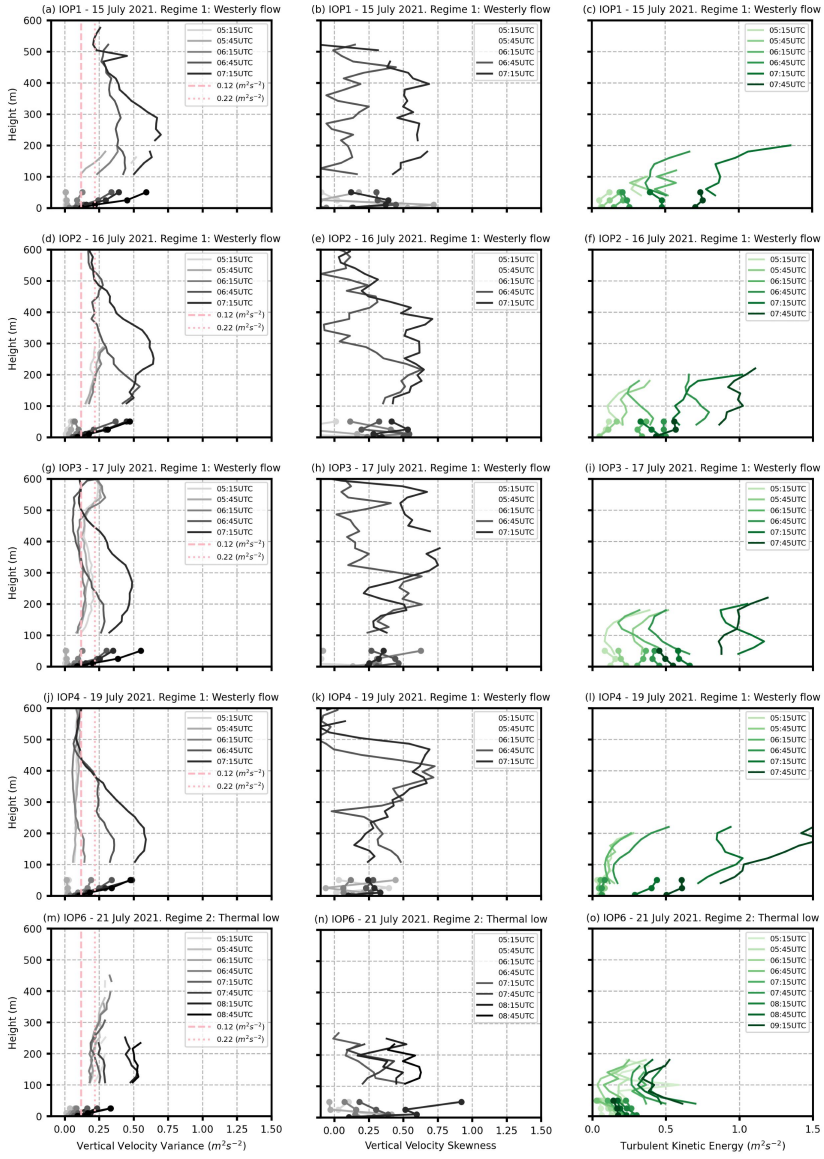


**FIGURE 5** (panels a, d, g, j, m) Observed vertical velocity variance profiles to a maximum height of 600 m from the Halo Doppler lidar and vertical velocity variance at 2 m, 10 m, 25 m and 50 m at the rainfed site (Els Plans, black). The vertical dashed line indicates the 0.12 $m^2$ $s^{-2}$ threshold from Hogan et al. (2009) which is applied to indicate convective onset at 50 m and the vertical dotted line indicates the 0.22 $m^2$ $s^{-2}$ threshold which is applied to indicate convective onset at 120 m and 200 m. (panels b, e, h, k, n) Observed vertical velocity skewness profiles to a maximum height of 600 m from the Halo Doppler lidar at the rainfed site (Els Plans, black). (panels c, f, i, l, o) TKE vertical profiles to a maximum height of 220 m from the Leosphere Windcube and TKE at 3 m, 25 m and 50 m at the irrigated site (La Cendrosa, green). Times are displayed in UTC. Due to instrumental issues only profiles from IOP1-4 (synoptic westerly flow cases) and IOP6 (thermal heat low case) are presented.

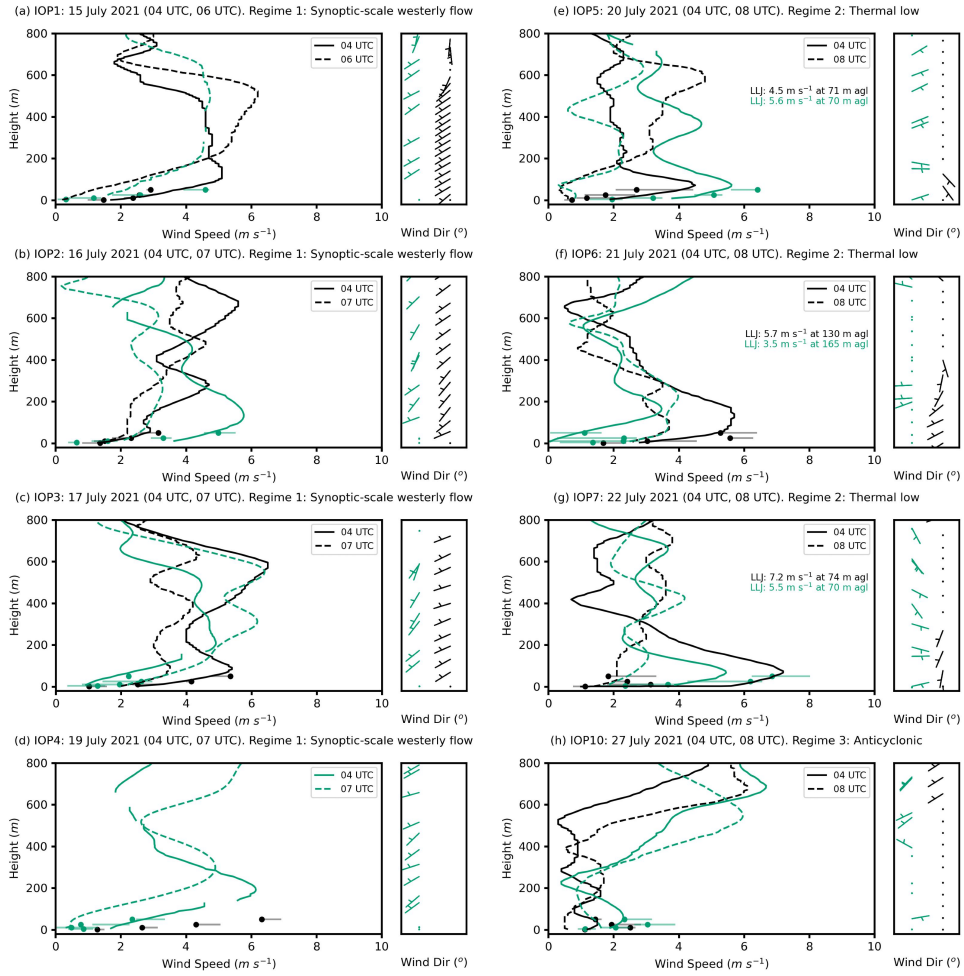


**FIGURE 6** Vertical profiles of wind speed and wind direction from radiosonde data on clear-sky IOP days are contrasted for the rainfed site (Els Plans, black) and irrigated site (La Cendrosa, green). Profiles are presented for the time nearest to sunrise (04 UTC) (solid line) and convective onset (dashed line). Observations from 2 m to 50 m are presented in each panel where the 30-min mean wind speed is shown by the marker and the standard deviation from 1-min data is presented by the horizontal bars. The vertical axis is height above the surface. Vertical profiles of wind direction are presented only for the time nearest to sunrise (04 UTC). Panels (e)-(g) includes the low-level jet (at 04 UTC) maximum wind speed and height for each site for IOP5–7. Times for the vertical profiles are displayed in UTC. NB on 15 July, vertical profiles are only available at convective onset for the irrigated site. NB on 19 July, vertical profiles are only available for the irrigated site.

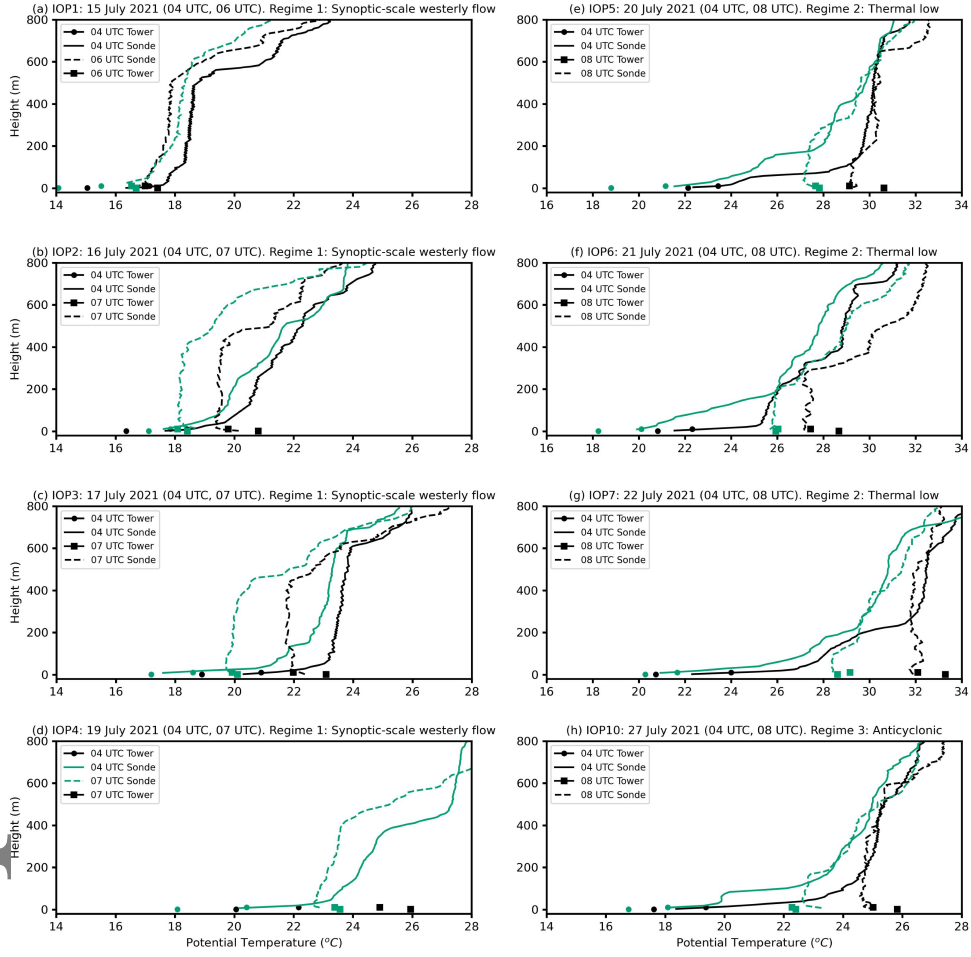


**FIGURE 7** Vertical profiles of potential temperature from radiosonde data on clear-sky IOP days contrasting the rainfed site (Els Plans, black) and irrigated site (La Cendrosa, green). Profiles are presented for the time nearest to sunrise (04 UTC) (solid line) and convective onset (dashed line). Observations at 2 m and 10 m are presented. Observations at 2 m and 10 m are presented in each panel where the 30-min mean potential temperature is shown by the marker for the rainfed site (Els Plans, black square) and irrigated site (La Cendrosa, green circle). The vertical axis is height above the surface. NB on 15 July, vertical profiles are only available at convective onset for the irrigated site. NB on 19 July, vertical profiles are only available for the irrigated site.

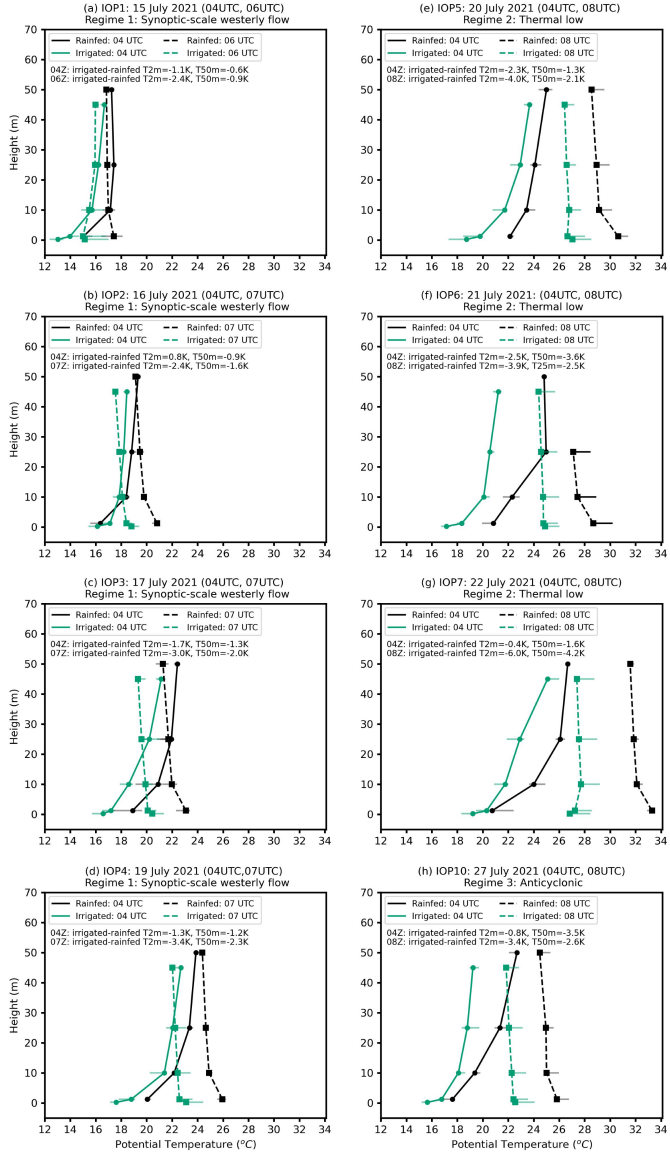


**FIGURE 8** Near-surface potential temperature from 2 m to 50 m on clear-sky IOP days are contrasted for the rainfed site (Els Plans, black) and irrigated site (La Cendrosa, green). Potential temperature at 0.2 m is also presented at the irrigated site. The 30-min mean potential temperature is shown by the marker and the standard deviation from 1-min data is presented by the error bars. Profiles are presented for the time nearest to sunrise (04 UTC) (solid line) and convective onset (dashed line). Temperature differences between irrigated and rainfed sites at 2 m and 50 m are stated.

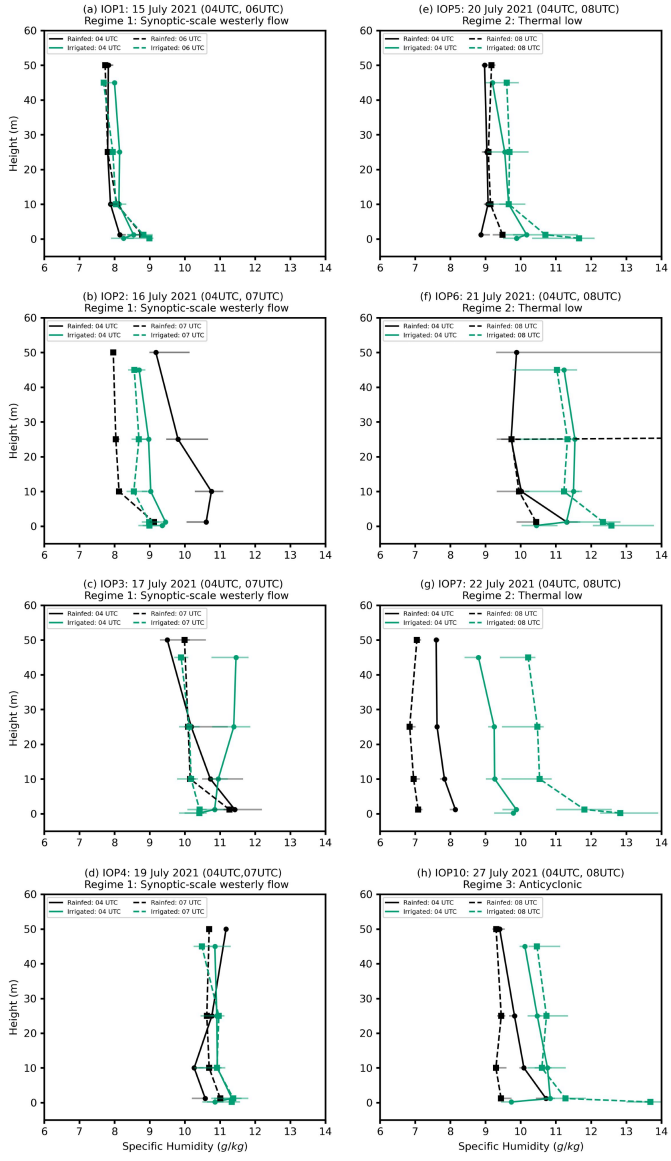


**FIGURE 9** Near-surface specific humidity from 2 m to 50 m on clear-sky IOP days contrasting the rainfed site (Las Plans, black) and irrigated site (La Cendrosa, green). Specific humidity at 0.2 m is also presented at the irrigated site. The 30-min mean specific humidity is shown by the marker and the standard deviation from the 1-min data is presented by the error bars. Profiles are presented for the time nearest to sunrise (04 UTC) (solid line) and convective onset (dashed line).